

1 **Tracking the Late Devonian high-P metamorphic belt in the**
2 **Variscan Orogen: new constraints on the PT evolution of**
3 **eclogites from the Cubito-Moura Unit (SW Iberian Massif)**

7 Irene Novo-Fernández^{a*}, Ricardo Arenas^a, Christian de Capitani^b, Manuel Francisco
8 Pereira^c, Rubén Díez Fernández^d, Sonia Sánchez Martínez^a, Antonio García-Casco^e

11 ^aDepartamento de Mineralogía y Petrología and Instituto de Geociencias (UCM, CSIC),
12 Universidad Complutense de Madrid. 28040 Madrid, Spain

13 ^bDepartment of Environmental Sciences (University of Basel). 4056 Basel, Switzerland

14 ^cDepartamento de Geociências (Universidade de Évora). Évora, Portugal

15 ^dDepartamento de Investigación y Prospectiva Geocientífica, Instituto Geológico y Minero
16 de España (IGME), Madrid, Spain

17 ^eDepartamento de Mineralogía y Petrología (University of Granada) and Instituto Andaluz
18 de Ciencias de la Tierra (UGR, CSIC), 18071, Granada, Spain

21 *Corresponding author at: Departamento de Mineralogía y Petrología. Facultad de Ciencias
22 Geológicas, Universidad Complutense de Madrid,
23 C/ José Antonio Novais, 12, 28040, Madrid, Spain

26 E-mail addresses:

27 inovo@ucm.es (Irene Novo-Fernández, corresponding author)

28 rarenas@ucm.es (Ricardo Arenas)

29 christian.decapitani@unibas.ch (Christian De Capitani)

30 mpereira@uevora.pt (Manuel Francisco Pereira)

31 r.diez@igme.es (Rubén Díez Fernández)

32 s.sanchez@geo.ucm.es (Sonia Sánchez Martínez)

33 agcasco@ugr.es (Antonio García-Casco)

39 **Abstract**

40 The Cubito-Moura Unit is a high-P metamorphic succession that occurs in the
41 southern part of the Ossa-Morena Complex (SW Iberian Massif). It includes a series of
42 metasedimentary, metafelsic and metamafic rocks affected by a high-P, low to
43 intermediate-T metamorphic event during Late Devonian times. Geochemistry of the
44 metabasic rocks reveals that the generation of the protoliths occurred in a supra-
45 subduction zone setting during Late Ediacaran to Early Ordovician times, either in a
46 back-arc or fore-arc context. The eclogites contain atoll-like garnets, omphacite,
47 amphibole, phengite (up to Si = 3.38 apfu), paragonite, rutile and quartz.
48 Thermodynamic modelling in the MnNCKFMASTH system indicates a high-P
49 metamorphic event at ~24 kbar and ~585°C followed by a thermal peak at ~19 kbar
50 and ~630°C, and a subsequent exhumation to ~15 kbar. This P-T path indicates deep
51 subduction at c. 370 Ma of this arc-related section. The lithostratigraphy and
52 tectonothermal evolution of the Cubito-Moura Unit are equivalent to that of a number
53 of units along the Iberian, Armorican and Bohemian massifs that can be correlated as a
54 part of the same Basal Allochthonous Terrane. These units define a single Late
55 Devonian high-P, low- to intermediate-T metamorphic belt developed during the first
56 stages of the Variscan Orogeny.

57

58 **Key-words:** Eclogites; Thermodynamic modelling; SW Iberian Massif; Variscan
59 Orogen; Variscan correlations

60

61

62 **1. INTRODUCTION**

63 Deep subduction of continental margins occurs in the initial stages of
64 continental collision. This process leads to the formation of distinctive high/ultrahigh-P
65 metamorphic belts, which are distributed along the suture zones of orogens and
66 contain key information on the nature of the paleo-subduction zones. Therefore, the

67 identification of high-P metamorphic belts is essential to understand the tectonic
68 evolution of orogens and plate margins (Dewey, 1975; Miyashiro, 1973). Along
69 Western and Central Europe, large outcrops of the Variscan Orogen define the French
70 Massif Central and Armorican, Bohemian and Iberian massifs (Fig. 1a). This orogenic
71 belt formed during the Devonian and Carboniferous as a consequence of the
72 diachronic collision between Gondwana and Laurussia which led to the assembly of
73 Pangea (Arenas et al., 2014; Díez Fernández et al., 2016; Franke, 1989, 2000; Kröner
74 and Romer, 2013; Martínez Catalán et al., 1997; Matte, 1991, 2001; Ribeiro et al.,
75 2007; Simancas et al., 2005). In the Iberian Massif, there is a complete transverse
76 cross-section of the Variscan Orogen, from the Gondwanan to the Laurussian
77 forelands (Fig. 1b). It includes an Internal Variscan Zone comprising ophiolites and
78 high-P units, which are preserved as tectonic klippen defining six allochthonous
79 complexes (i.e. Cabo Ortegal, Órdenes, Malpica-Tui, Bragança, Morais and Ossa-
80 Morena) featured by several suture zones exposures (Fig. 1b; Arenas et al., 2016a;
81 Díez Fernández et al., 2016; Martínez Catalán et al., 2009).

82

83 In NW Iberian Massif, the allochthonous complexes comprise a thick stack of
84 terranes (Fig. 1b). At the top of the nappe pile, a peri-Gondwanan continental-affinity
85 terrane, so-called Upper Units, traces an Early Devonian high-P, high-T metamorphic
86 belt (Ábalos et al., 2003; Fernández-Suárez et al., 2007; Fuenlabrada et al., 2010; Gil
87 Ibarguchi et al., 1990; Mendía et al., 2001; Ordóñez Casado et al., 2001). It occurs
88 above a group of Ophiolitic Units that define a complex Variscan suture zone (Arenas
89 and Sánchez Martínez, 2015). At the base of the allochthonous complexes, there is
90 another terrane of peri-Gondwanan affinity that experienced Late Devonian high-P,
91 low- to intermediate-T metamorphism, the so-called Basal Units (Abati et al., 2010;
92 Arenas et al., 1995; Díez Fernández et al., 2011; Gil Ibarguchi and Ortega Gironés,
93 1985; Martínez Catalán et al., 1996; Munhá et al., 1984; Rodríguez et al., 2003).

94

95 In the SW Iberian Massif, the Ossa-Morena Complex has been classically
96 interpreted as an autochthonous paleogeographic domain. However, during the last
97 decades tectonic units that developed high-P metamorphism in the Late Devonian
98 have been identified within this domain (Ábalos et al., 1991; Abati et al., 2018; Azor et
99 al., 1994; Fonseca et al., 1999; Leal, 2001; Mata and Munhá, 1986; Moita et al., 2005;
100 Pedro, 1996; Pereira et al., 2010; Rosas et al., 2008). This led to a proposal of
101 correlation along the Iberian Massif of the units affected by a Late Devonian high-P,
102 low- to intermediate-T metamorphic event, which would define a Basal Allochthonous
103 terrane all through Iberia (Arenas et al., 2016a; Díez Fernández and Arenas, 2015;
104 Díez Fernández et al., 2016).

105

106 In NW Iberia, the PT evolution of the Basal Units is rather well constrained
107 (Arenas et al., 1995; Gil Ibarguchi and Ortega Gironés, 1985; Gil Ibarguchi, 1995; Li
108 and Massone, 2016, 2017; Li et al., 2017; López Carmona et al., 2010, 2013, 2014;
109 Puelles et al., 2017; Rubio Pascual et al., 2002). Nevertheless, the metamorphic
110 evolution of the Late Devonian high-P, low- to intermediate-T Basal Units of SW Iberia,
111 including the Badajoz-Córdoba (BCU) and the Cubito-Moura (CMU) units (Fig. 1b), is
112 less well known. Arenas et al. (In press) have presented detailed thermodynamic
113 modelling of unusual Mg-rich chloritoid-bearing high-P metapelites from the BCU.
114 However, the most common high-P rocks in this tectonic unit are severely retrogressed
115 eclogites (Ábalos et al., 1991; Abati et al., 2018; López Sánchez-Vizcaíno, 2003; Mata
116 and Munhá, 1986; Pereira et al., 2010). In the CMU, the high-P rocks of the Évora
117 Massif and further south (Fig. 1b), are better preserved than those of the BCU, and
118 some qualitative constraints regarding their PTt evolution have been published (Moita et
119 al., 2005; Rosas et al., 2008). In this paper we update this information by means of
120 thermodynamic modelling.

121

122 The contrasting metamorphic information available for the sequences grouped
123 into the Basal Allochthonous Units demand new research in order to achieve a
124 coherent view of the entire Late Devonian metamorphic belt. The aim of this work,
125 which includes whole-rock geochemistry and mineral chemistry of the Safira eclogites,
126 and thermodynamic modelling in the MnNCKFMASHT system, is to constrain the
127 nature of the protoliths and the PT evolution followed by these rocks of the CMU. In
128 addition, our findings are compared with the tectonothermal evolution of the high-P
129 units from NW and SW Iberia to test tectonic correlations, and to provide far-reaching
130 conclusions regarding the structure and dynamics of the associated subduction
131 channel system active during the Late Devonian.

132

133 **2. GEOLOGICAL SETTING**

134 **2.1 Basal Units: SW Iberian Massif**

135 In SW Iberian Massif, the Ossa-Morena Complex contains two Late Devonian
136 high-P, low- to intermediate-T units (Basal Units) with a NW-SE trend: the Badajoz-
137 Córdoba Unit (BCU) to the north (also known as Central Unit; Fig. 1b) and the Cubito-
138 Moura Unit (CMU) to the south (Fig. 1b).

139

140 **2.1.1 Badajoz-Córdoba Unit**

141 The BCU and CMU (Fig. 1b) have the same tectonostratigraphic position within
142 the allochthonous pile (Díez Fernández and Arenas, 2015). The BCU is divided into
143 two sequences (Azor et al., 1994). The Lower Sequence contains albite-bearing
144 paragneisses alternating with minor quartzites and marbles, with abundant alkaline and
145 calc-alkaline orthogneisses and metabasites. The Upper Sequence is composed by
146 micaschists, garnet-bearing micaschists and orthogneisses. Protolith ages of the felsic
147 gneisses and metabasites range from c. 577 to 480 Ma, and from c. 615 to 585 Ma,
148 respectively (Abati et al., 2018). The BCU was affected by high-P, low- to intermediate-

149 T metamorphism dated at c. 377 Ma (Abati et al., 2018), reaching peak-P conditions at
150 c. 20 kbar and 525°C (Arenas et al., In press).

151

152 2.1.2 Cubito-Moura Unit

153 The CMU extends along two hundred kilometers from the Évora Massif to the
154 north of the Aracena Massif and is divided into two juxtaposed sequences according to
155 their lithostratigraphy (Díez Fernández and Arenas, 2015; Díez Fernández et al.,
156 2016). The Lower Sequence is found in the Évora Massif, and further south in the
157 Alvito-Viana do Alentejo sector (Fig. 1b). The Évora Massif is a large dome-like
158 structure located in the westernmost part of the Ossa-Morena Complex (Dias da Silva
159 et al., 2018; Pereira et al., 2009). It is composed of two domains: a high-grade domain
160 (footwall block) separated from an overlying low- to intermediate-grade domain
161 (hanging-wall block) by extensional shear zones (Dias da Silva et al., 2018; Pereira et
162 al., 2003, 2007, 2009) (Fig. 2). The high-grade metamorphic domain appears in the
163 core of late upright antiforms and comprises gneisses, migmatites and amphibolites
164 closely associated with gabbro-diorites and granitic rocks dated at c. 341-336 Ma
165 (Moita et al., 2015; Pereira et al., 2015). In the Montemor-o-Novo - Safira area, the low-
166 to-intermediate-grade metamorphic domain appears in the core of the late upright
167 synforms where the Lower Sequence of the Basal Units occurs, such as the Cabrela-
168 Carvalhal synform (Fig. 2), representing a later contractional structure (Chichorro,
169 2006; Díez Fernández et al., 2017; Pereira et al., 2007, 2009). The Lower Sequence
170 includes metasedimentary, metafelsic and, in less proportion, metamafic rocks variably
171 distributed in two members (Fig. 2). The lower member (Escoural Unit or Serie Negra
172 Group; Chichorro, 2006; Chichorro et al., 2008), comprises metapelites,
173 metagreywackes, paragneisses, micaschists, black metacherts and black quartzites,
174 with maximum depositional ages around 560-540 Ma (Late Ediacaran; Pereira et al.,
175 2008). These metasedimentary rocks are associated with amphibolites and abundant
176 felsic gneisses yielding a protolith age of c. 522-517 Ma (Early Cambrian; Chichorro et

177 al., 2008). The upper member (Monfurado Unit), comprises micaschists, meta-arkoses,
178 marbles and interbedded metafelsic and metamafic rocks, assigned to the Early-Middle
179 Cambrian (Chichorro, 2006; Pereira et al., 2007). Geochronological and geochemical
180 features of the Late Ediacaran metasedimentary rocks (i.e. Escoural Unit) suggest a
181 depositional environment in a basin related to the erosion of a Cadomian magmatic arc
182 in the Gondwanan margin, with strong contribution from the West African Craton
183 (Chichorro et al., 2008; Díez Fernández et al., 2017; Pereira et al., 2008). Later,
184 siliciclastic and carbonate sediments and volcanic rocks (i.e. Monfurado Unit)
185 deposited as a result of a Cambrian rifting process (Chichorro et al., 2008; Pereira et
186 al., 2007).

187

188 In the Évora Massif, the Lower Sequence of the Basal Units is tectonically
189 overlain by the Carvalhal Unit (Carvalhosa and Zbyszewski, 1994) (Fig. 2) representing
190 an igneous (mafic-dominated) and sedimentary complex (Chichorro, 2006; Pereira et
191 al., 2007), interpreted as a Middle Cambrian-Ordovician (?) ophiolitic unit (Díez
192 Fernández et al., 2017).

193

194

195 **2.2 Basal Units: NW Iberian Massif**

196 The Basal Units in NW Iberian Massif (Galicia) are divided into two tectonically
197 juxtaposed sequences according to their lithostratigraphy (Díez Fernández et al.,
198 2010). The Lower Sequence is composed by siliciclastic metasediments of Late
199 Ediacaran age (c. 560-540 Ma, U-Pb in detrital zircon; Díez Fernández et al., 2010).
200 The Upper Sequence includes siliciclastic metasediments and marbles, with a Middle-
201 Late Cambrian maximum depositional age (c. 512-480 Ma, U-Pb in detrital zircon; Díez
202 Fernández et al., 2010, 2013). These sediments were intruded by Cambrian-
203 Ordovician calc-alkaline granitoids and mafic dykes (c. 498-493 Ma; Abati et al. 2010;
204 Andonaegui et al., 2017) and by a suite of peralkaline affinity (c. 482-470 Ma; Díez

205 Fernández et al., 2012a; Montero et al., 2009). The Basal Units in NW Iberia are
206 considered the remnants of a Cadomian peri-Gondwanan back-arc located at the
207 eastern part of the West African Craton affected by a Cambrian rifting episode (Díez
208 Fernández et al., 2010; Fuenlabrada et al., 2012).

209

210 The PT conditions experienced during Late Devonian times (c. 377-372 Ma;
211 Abati et al., 2010; Beranoaguirre et al., 2019; Rodríguez et al., 2003) by the Basal
212 Units in NW Iberia correlate, in general, with their tectonostratigraphic division. In the
213 Lower Sequence, PT conditions increase progressively to the west, from the
214 blueschists to intermediate-T eclogite facies, as a likely consequence of different
215 original position of tectonic units in a W-dipping subducting slab (present coordinates,
216 Martínez-Catalán et al., 1996; Díez Fernández et al., 2012b). The Upper Sequence is
217 characterized by blueschist facies metamorphism at the base, while high-P
218 metamorphism has not been identified at the top of the sequence (López-Carmona et
219 al., 2010, 2013, 2014; Rodríguez et al., 2003). The colder metamorphic evolution of the
220 Upper Sequence has been attributed to the regional scale depression of isotherms
221 during the subduction channel dynamics (Díez Fernández et al., 2011).

222

223 **3. HIGH-P METAMORPHISM IN THE CMU: BACKGROUND**

224 In the CMU, Fonseca et al. (1993), Leal (2001), Moita (1997), Pedro (1996) and
225 Rosas (2003) reported blueschists and eclogites in the Évora Massif (i.e. Montemor-o-
226 Novo – Safira area), and further south (Alvito-Viana do Alentejo area). They are
227 interpreted to represent a Variscan high-P and low- to intermediate-T metamorphic
228 event at c. 371 Ma (Sm-Nd whole rock-garnet isochron; Moita et al., 2005). In spite of
229 the detailed descriptions of these high-P metamafic rocks, their PT conditions and
230 paths remain poorly constrained.

231

232 In the Montemor-o-Novo - Safira area, meter-scale lenses of eclogites mainly
233 composed of garnet, omphacite and white mica, locally with glaucophane, are found
234 surrounded by felsic gneisses and micaschists (Leal, 2001; Pedro, 1996). A major
235 feature of the Safira eclogites is the atoll-shaped garnets, which are not recognized in
236 the Alvito-Viana do Alentejo eclogites (Leal, 2001). Minimum-T of 520-620 °C and
237 minimum-P of 10-13 kbar were estimated for the metamorphic peak of the Safira
238 eclogites using thermobarometry (Leal, 2001; Pedro, 1996).

239

240 In the Alvito-Viana do Alentejo area, variably retrogressed glaucophane-bearing
241 eclogites and blueschists occur as meter-scale lenses within metapelites, marbles and
242 gneisses (Moita, 1997; Leal, 2001). The eclogites are mainly composed of garnet,
243 omphacite, and glaucophane, and include white mica, quartz and rutile as accessories,
244 whereas blueschists consist mostly of garnet and glaucophane. PT conditions of 10 to
245 16 kbar and 450-650°C for the metamorphic peak of the glaucophane-bearing eclogites
246 were estimated by Moita (1997) via classical thermobarometry. Also, pseudosection
247 modelling was performed by Leal (2001) in the NCFMASH system, which yielded 650-
248 700 °C and 18 kbar for the metamorphic peak. On the other hand, Moita (1997)
249 inferred lower pressures of 10-12 kbar in the blueschists based on the classical stability
250 fields for blueschists proposed by different authors.

251

252 **4. METHODS**

253 **4.1 Mineral chemistry**

254 The mineral chemistry of two fresh samples of the Safira eclogites was
255 investigated to estimate their P-T conditions of metamorphism and decipher their
256 tectonothermal evolution. Elemental X-Ray maps of the two eclogite samples were
257 obtained with a JEOL Superprobe JXA-8900M from Universidad Complutense (Madrid,
258 Spain). The microprobe was operated at 300 nA beam current, 20 kV accelerating
259 voltage, 2 µm pixel size and 20 ms counting time, to acquire (by means of wavelength

260 dispersive spectrometry, WDS) X-Ray maps of Si (K α), Ti (K α), Al (K α), Fe (K α), Mn
261 (K α), Mg (K α), Ca (K α), Na (K α) and K (K α). The images were processed with
262 DWImager software (Torres-Roldán and Garcia Casco, 2003, unpublished see Garcia-
263 Casco, 2007). As shown in the figures, the X-Ray maps were masked for polish
264 defects, voids and selected minerals in order to better show the textural-chemical
265 features of the mineral of interest. Furthermore, manipulation of several histograms at a
266 time allowed to create phase maps, and to obtain the abundance of the minerals. The
267 elemental maps were quantified applying an internal mineral standard selected among
268 the analyzed minerals in the scanned area after the acquisition of the X-Ray maps. The
269 quantification follows the Bence and Albee (1968) scheme, and the α -factor table by
270 Kato (2005). Each pixel in the quantified maps corresponds to a mineral analysis
271 expressed as color-coded atoms per formula unit or atomic ratios. $Fe^{2+} = Fe_{Total}$ in the
272 quantified maps. A grey-scale base-layer, calculated with the expression:

$$\sum counts * A_i$$

273 (where A is atomic number, and i is Si, Ti, Al, Fe, Mn, Mg, Ca, Na, K and P) underlies
274 the masked areas of the X-Ray maps. This layer contains the basic textural information
275 of the scanned areas. Spot analyses were performed on the scanned areas and other
276 significant areas of the thin sections. The operation conditions were 20 kV accelerating
277 voltage and 20 nA beam current, and the PAP correction procedure was used
278 (Pouchou and Pichoir, 1985). Structural formulas of minerals were normalized to 12, 11
279 and 2 oxygens for garnet, white mica and rutile, respectively. The structural formula of
280 pyroxene was normalized to 6 oxygens following the procedure proposed by Morimoto
281 (1988). The structural formula of amphiboles was normalized to 23 oxygens using the
282 method of Schumacher (in Leake et al., 1997) and follows the classification scheme of
283 Leake et al. (1997). The atomic concentration of elements per formula units is
284 abbreviated apfu. Mg# is the abbreviation of the Mg number ($Mg/(Mg+Fe^{2+})$). Mineral
285 abbreviations are after Whitney and Evans (2010). Projection after coexisting phases

287 and condensation along exchange vectors of the multidimensional chemical space has
288 been performed using CSpace software (Torres-Roldan et al., 2000) in order to
289 produce tetrahedral diagrams (ACFN deluxe diagram, Garcia-Casco et al., 2013,
290 based on the ACF diagram of Thompson, 1982) containing the full mineralogical
291 information of the samples. The compositions of analyzed garnet, clinopyroxene,
292 amphibole, white mica and plagioclase from the two samples of eclogite are listed in
293 Tables S1-S4 (Data Repository).

294

295 **4.2 Whole-rock geochemistry**

296 Whole-rock chemical analyses of 12 fresh samples of eclogite from the Montemor-o-
297 Novo - Safira and Alvito-Viana do Alentejo areas were performed at ActLabs
298 laboratories (Ontario, Canada). Lithium metaborate/tetraborate fusion was employed,
299 and samples were analyzed by Inductively Coupled Plasma analysis (ICP-OES and
300 ICP-MS). In major elements, the precision of the analysis is 0.01%, with MnO and TiO₂
301 reaching 0.001%. The precision of the trace elements is ranges from 0.002 to 30 ppm.
302 Major and trace elements, including REE, of the eclogite samples are listed in Table S5
303 (Data Repository) and represented in Fig. 11.

304

305 **5. RESULTS**

306 **5.1. Petrography and mineral chemistry**

307 The Safira eclogites occur as variably retrogressed lenses of variable size
308 surrounded by metasedimentary rocks and ortogneisses (Fig. 2). The lenses usually
309 contain a well-preserved central zone surrounded by a retrogressed rim (Leal, 2001).
310 The host metamorphic rocks show a post-eclogitic regional foliation
311 (amphibolite/greenschists facies) probably related to the exhumation of the high-P unit
312 (Chichorro, 2006; Pereira et al., 2007). Samples 116748 and 116747 of the Safira
313 eclogites were selected for detailed study. They show a well-preserved mineral
314 assemblage that allows deducing the metamorphic peak.

315

316 **5.1.1 Sample 116748**

317 Sample 116748 is a very fine-grained isotropic eclogite. It consists of garnet
318 (~26 vol.%), clinopyroxene (~40 vol.%) and amphibole (~21 vol.%), with phengite (~3
319 vol.%), paragonite (~0.25 vol.%), rutile (~2 vol.%), quartz (~1 vol.%), apatite (~0.5
320 vol.%), dolomite (~0.1 vol.%) and pyrite (~0.2 vol.%) as accessory phases (Fig. 3a, b).

321

322 Garnet commonly occurs as fine-grained idioblastic to subidioblastic atoll-like
323 crystals (up to 0.4 mm in size), although non-atoll-like blasts are found locally
324 (hereinafter referred to as 'complete' garnet). X-Ray maps show well differentiated
325 garnet core and rim domains (Fig. 4). Garnet cores (hereinafter referred to as garnet I;
326 ~15 vol.%) in both, atoll and 'complete' blasts, have a compositional zoning
327 characterized by outward decreasing Ca and Mn, and increasing Mg (Figs. 4c-f, 5b).
328 Garnet rims (hereinafter referred to as garnet II; ~11 vol.%) show patchy zoning, and
329 have lower Ca and higher Mg contents compared to garnet I (Figs. 4c-f, 5b; Table S1).
330 Fe increases from garnet I to II, locally displaying patchy distribution in both (Fig. 4f).
331 Mn content in garnet II is similar to the concentration in garnet I cores (Fig. 4d). Within
332 the 'complete' garnet crystal shown in Fig. 4c-f, an 'island' (in the sense of Fayard et
333 al., 2010) with the same composition of garnet II occurs. This garnet crystal also shows
334 a 'peninsula' linked to garnet II (Fig. 4a, c-f). In addition to rings surrounding garnet I
335 and islands and peninsulas in 'complete' garnet blasts, garnet II also occurs as small
336 grains usually within the atoll structures or connecting different atoll crystals (Fig. 4a, c-
337 f). Fig. 3e shows the presence of microveins connecting garnet I and II that show
338 almost identical image contrast to that of garnet II. Both, garnet I and II are of
339 almandine-rich composition (garnet I: Alm₅₁₋₅₇ Grs₂₅₋₃₄ Prp₁₂₋₁₉ Sps₁; garnet II: Alm₅₂₋₅₃
340 Grs₁₈₋₂₂ Prp₂₁₋₂₃ Sps₁₋₂; Table S1; Fig. 5a) and include rutile and quartz, and locally
341 omphacite is found within garnet I. . The mineral paragenesis found within the atoll

342 structure comprises mostly amphibole, phengite and quartz, although small crystals of
343 omphacite, rutile, and apatite also occur (Fig. 4a).

344

345 Clinopyroxene is the most abundant mineral in the matrix, although it also
346 appears as tiny crystals inside the atoll garnet rings. Locally it occurs associated with
347 garnet II islands within garnet I. It is classified as omphacite, with most omphacite
348 crystals showing weak zoning (Fig. 4g) with increasing jadeite contents from cores
349 (41.2 mol.%) to rims (53.4 mol%) (Table S2; Fig. 5d,e). The X-Ray maps show
350 omphacite inside the atoll garnets with the same chemical composition as the rims of
351 matrix omphacite (Fig. 4g). Aegirine content in omphacite ranges from 0 mol.% to 9
352 mol.%.

353

354 Amphibole occurs in both, matrix and inside atoll garnet rings. It is green-
355 colored in plane polarized light (Fig. 3a) and of relatively uniform barroisite composition
356 ($\text{Si} = 6.84\text{-}7.29 \text{ apfu}$; $\text{Al(C)} = 1.25\text{-}1.44 \text{ apfu}$; $\text{Na(B)} = 0.89\text{-}1.33 \text{ apfu}$; $\text{Na+K(A)} = 0.34\text{-}$
357 0.48 ; $\text{Mg\#} = 0.71\text{-}0.76$; Fig. 5h; Table S3), although some crystals show a weak zoning
358 with rims richer in Ca, Fe and Al contents, and poorer in Na and Si contents.

359

360 Phengite appears in the matrix and encompassed by atoll garnet rings. When in
361 the matrix, it shows a xenoblastic habit, as opposed to well-developed crystal faces
362 when inside atoll garnet rings, except for the faces in contact with garnet, which follow
363 the shape of garnet (Fig. 4a). Matrix phengite does not show inclusions, whereas
364 phengite within atoll garnet includes rutile, quartz, apatite, garnet I and garnet II (Fig.
365 4a). Phengite exhibits no zoning and there is no compositional difference between the
366 two textural types. Si content is high and ranges between 3.25 and 3.31 apfu (Table
367 S4; Fig. 5g). Paragonite occurs exclusively in the matrix as idioblastic to subidioblastic
368 grains that may contain garnet I and II inclusions. Na and K contents range from 0.66
369 to 0.87 apfu and from 0.04 to 0.09 apfu, respectively (Table S4).

370
371 Rutile crystals occur in the matrix with tens of micrometers to ~0.2 mm in size.
372 Rutile grains a few micrometers in size are found also within the atoll garnet rings.
373 Besides, it also appears as inclusion in both, garnet I and II. Quartz is present in the
374 matrix as fine grains and inside the atoll garnet with up to 0.1 mm in size. Fine-grained
375 dolomite is considered retrograde, for it appears in the matrix usually close to late
376 amphibole or associated with late amphibole in fractures within omphacite.

377
378 Textural and chemical relations allow defining a first mineral assemblage
379 consisting of garnet I, omphacite cores, rutile, quartz and phengite that was followed by
380 the metamorphic peak mineral assemblage composed by garnet II, omphacite rims,
381 quartz, rutile and phengite. Finally, paragonite, barroisite and dolomite formed during
382 retrogression.

383

384 **5.1.2 Sample 116747**

385 Sample 116747 is a very fine-grained isotropic eclogite. Compared to sample
386 116748 it has lower volumes of garnet (~18 vol.%), clinopyroxene (~28 vol.%),
387 phengite (~0.2 vol.%), rutile (~1.5 vol.) and quartz (<1 vol.%), and higher volumes of
388 amphibole (~45 vol.%), paragonite (~1.5 vol.) and plagioclase (~1.5 vol%) (Fig.
389 3c,d).

390

391 Garnet occurs as fine idioblastic to subidioblastic atoll-like crystals with
392 maximum crystal sizes of 0.3 mm. As in sample 116748, two well differentiated
393 domains are recognized using X-Ray maps (Fig. 4b,h-j). Garnet atoll structure has a
394 greater development in this sample compared to sample 116748, with a lower volume
395 of garnet I (~9 vol.%, Fig. 4b). Yet, zoning is recognized (Fig. 5c), with Ca content
396 decreasing towards the outermost part of garnet I while Mg content increases (Fig. 4h).
397 Due to the larger development of atoll structures, it is more difficult to identify a zoning

398 pattern in Mn content, although some crystals show slight depletion towards the
399 outermost part of garnet I (Fig. 4i). Fe does not show zoning in garnet I (Fig. 4j). On the
400 other hand, garnet II occurs as rings surrounding garnet I or as xenoblastic crystals in
401 the matrix (Fig. 4b). Garnet II is not zoned, and it has lower Ca and higher Mg and Mn
402 contents than garnet I (Fig. 4h,i). Fe is slightly higher in garnet II (Fig. 4j). As in sample
403 116748, garnet show microveins connecting garnet I with garnet II, but with a greater
404 development (Fig. 3f). The mineral paragenesis developed within the atoll structure is
405 composed of amphibole, omphacite, phengite and fine crystals of rutile, garnet II, and
406 apatite (Fig. 4b). Both garnet I and II are of almandine-rich composition (garnet I: Alm₅₁-
407 ₆₁ Grs₂₂₋₄₀ Prp₆₋₁₁ Sps₁₋₂; garnet II: Alm₆₀₋₆₁ Grs₁₉₋₂₂ Prp₁₇₋₁₉ Sps₂₋₃; Table S1; Fig. 5a).

408

409 Clinopyroxene in the matrix and inside atoll garnet (Fig. 4k) is of omphacite
410 composition (Table S2; Fig. 5d). Grains in the matrix show cores poorer in jadeite (37.3
411 mol.%) than in the rims (55.2 mol.%) (Fig. 5f; Table S2), while omphacite inside atoll
412 garnet shows no zoning and is similar in composition to matrix omphacite rims (Fig.
413 4k). The aegirine content ranges between 1.5 and 13.3 mol.%.

414

415 Amphibole grains appear zoned in sample 116747. In the matrix and inside atoll
416 garnet rings, bluish amphibole (Fig. 3c) classified as glaucophane (Si = 7.25-7.69 apfu;
417 Na(B) = 1.51-1.77 apfu; Mg# = 0.64-0.75; Table S3; Fig. 5j) is predominant. In the
418 matrix, glaucophane cores evolve to barroisite towards rims of grains, with higher Al,
419 Fe, Ca and K, and lower Si, Mg and Na content (Si = 6.95-7.37 apfu; Al(C) = 1.36-1.66
420 apfu; Na(B) = 0.76-1.48 apfu; Na+K(A) = 0.29-0.47; Mg# = 0.60-0.67; Table S3; Fig.
421 5h). Locally, amphibole rims exhibit still higher Al, Ca and K and lower Si, Mg and Na
422 contents and classify as magnesiokatophorite (Si = 6.50-6.88 apfu; Na(B) = 0.81-1.02
423 apfu; Na+K(A) = 0.51-0.67; Mg# = 0.56-0.66; Table S3; Fig. 5i). Magnesiokatophorite
424 also overgrowths omphacite and is associated with late plagioclase.

425

426 Phengite is scarce and mainly occurs within atoll garnet rings, usually with well-
427 developed faces, although very fine grains (tens of micrometers in size) with irregular
428 faces occur in the matrix (Fig. 4b). Both types of phengite do not show inclusions and
429 compositional differences, with Si content ranging between 3.27 and 3.38 apfu (Table
430 S4, Fig. 5g). Paragonite occurs in the matrix as large subidioblastic crystals (up to 0.45
431 mm in length) with Na content ranging between 0.68 and 0.94 apfu (Table S4).
432 Plagioclase is of albite composition ($Ab = 98.2\text{-}98.9$ mol.%; Table S4) and replaces
433 omphacite and is associated with magnesiokatophorite.. Rutile occurs in the matrix
434 (~0.1 mm in size) and within atoll garnet (very fine crystals).

435

436 According to textural relationships and mineral composition, garnet I, omphacite
437 cores, glaucophane, rutile and phengite formed a first paragenesis that was followed by
438 the metamorphic peak paragenesis composed by garnet II, omphacite rims,
439 glaucophane, quartz, rutile and phengite. During retrogression, barroisite and
440 paragonite formed first shortly before albite and magnesiokatophorite. The mineral
441 assemblage development for this sample is presented in Fig. 6 and the corresponding
442 ACFN diagrams of Fig. 7. In the latter, the composition of the sample and coexisting
443 minerals are shown, while the tie-lines connecting mineral analyses represent
444 equilibrium during the different stages of metamorphism.

445

446 **5.2. Isochemical phase diagrams**

447 Isochemical phase diagrams were calculated for samples 116748 and 116747
448 in the MnNCKFMASTH system using the software Theriaik-Domino (De Capitani and
449 Brown, 1987; De Capitani and Petrakakis, 2010). The internally consistent database
450 5.5 of Holland and Powell (1998; updated November 2003) was used (database
451 “tcdb55c2d” and input “THERIN” are provided in the supplementary material). Activity-
452 composition models were considered for clinopyroxene (Green et al., 2007), garnet,
453 biotite, ilmenite, spinel (White et al., 2007), amphibole (Diener et al., 2007),

454 orthopyroxene (White et al., 2002, 2007; also in Baldwin et al., 2005), white mica
455 (Coggon and Holland, 2002), feldspar (Baldwin et al., 2005), epidote, talc and chlorite
456 (Holland and Powell, 1998). Pure phases used in the calculation include quartz/coesite,
457 rutile, lawsonite and titanite (Holland and Powell, 1998). Calculations were performed
458 assuming H₂O in excess. The compositions used for the calculation are reported in
459 Table 1. Calculations were made in a P-T window from 5 to 30 kbar and 500 to 650 °C.
460 Both samples yielded almost identical results. Below, we offer the thermodynamic
461 modelling of sample 116747, while results for sample 116748 are provided in the
462 supplementary material (Fig. S1).

463

464 **5.2.1 Sample 116747**

465 Results for this sample are shown in Fig. 8. The peak assemblage
466 (Grt+Omp+Gln+Ph+Qz+Rt) is stable from 570 to 650 °C and from 16 to 27 kbar. Si-in-
467 phengite isopleths constrains pressure to 18-20 kbar (Si = 3.27-3.38 apfu; Fig. 8b). The
468 distribution of garnet isopleths (Fig. 8c-e) reproduces the observed decrease in
469 grossular content (0.22 to 0.30) and the increase in pyrope (0.11 to 0.15) and
470 almandine contents (0.58 to 0.61) in pre-peak garnet I, constraining initial PT
471 conditions to c. 570 °C and c. 19 kbar. The prograde evolution, constrained by zoning
472 of garnet I, trends towards a maximum pressure of ~24 kbar constrained by the almost
473 isobaric isopleths of almandine ($X_{\text{Alm}} = 0.61$) while grossular and pyrope isopleths (X_{Prp}
474 = 0.15; $X_{\text{Grs}} = 0.22$) constrain the temperature of pressure peak to 580 °C,
475 corresponding to outermost part of garnet I. This estimation is consistent with the
476 increase in Al observed in omphacite (Fig. 8f).

477

478 For stage 2 of mineral assemblage development (Figs. 6 and 7), the
479 intersection of Si-in-phengite (within the atoll structures, $Si_{\text{max}} = 3.38$ apfu) with
480 grossular (0.19-0.22), pyrope (0.17-0.19) and almandine (0.60-0.61) isopleths for
481 garnet II yield 615-640°C and 18-20 kbar (Fig. 8 and 9). Some garnet analysis with

482 lower grossular, and higher pyrope and almandine contents do not intersect the
483 maximum Si content in phengite in the stability field of the peak mineral assemblage
484 (stage 2). This may be due to analytic errors, uncertainties in the standard state
485 properties of end-members and solution models and/or problems with the effective bulk
486 composition (e.g. fractionation during the growth of garnet and clinopyroxene).
487 Phengite from the matrix and within the atoll structure shows the same chemical
488 composition, indicating re-equilibration during this stage. Moreover, omphacite within
489 atoll structures and rims of matrix omphacite show the same composition, and
490 isopleths of Al content in clinopyroxene show that it was formed at the highest
491 temperature reached (Fig. 8f). Hence, we conclude that stage 2 developed upon
492 decompression and heating after stage 1 (Fig. 9). Finally, stage 3 paragonite grew
493 during decompression (Figs. 8 and 9), when albite, barroisite and magnesiokatophorite
494 formed at the expense of omphacite. This mineral paragenesis points to a pressure
495 below 15 kbar, although the temperature cannot be constrained. However, volume
496 isopleths for garnet (19%), omphacite (28%), amphibole (45%) and plagioclase (2%)
497 intersect at 14-15 kbar in the range of 625-640°C (Fig. 10a-d), which is considered a
498 rough estimation of the temperature of arrest of reaction progress in the sample. A
499 similar evolution is inferred for sample 116748 (Fig. S1).

500

501 **5.3. Whole-rock geochemistry**

502 Major and trace element composition of eclogites from the CMU allow rock
503 classification and determination of the tectonic setting of formation of their protoliths.
504 Four of the samples were collected in the Montemor-o-Novo - Safira area, and eight in
505 the Alvito-Viana do Alentejo area. Eclogite samples exhibit a limited variation in their
506 major elements and they have a relatively low Mg#, in the range of 0.26 to 0.48 (Table
507 S5). Immobile elements have been used for classification in order to minimize the
508 effect of possible element mobility during alteration and/or metamorphism (Pearce,
509 2014). In terms of Zr/Ti-Nb/Y diagram (Pearce, 1996), all of the high-P rocks fall in the

510 basalt field, although two samples are in the limit of basalt and andesite + basaltic
511 andesite fields, and all of them display subalkaline nature ($\text{Nb/Y} = 0.02$ to 0.51 , $\text{Zr/Ti} =$
512 0.008 to 0.017 ; Table S5, Fig. 11a).

513

514 The tectonic setting of the protoliths was determined following the procedure
515 proposed by Pearce (2014). Fig. 11b shows N-MORB normalized (Sun and
516 McDonough, 1989) immobile-element patterns of analyzed samples. Due to their
517 similar behavior, pairs of elements Nb-Ta, Hf-Zr and Ho-Y are plotted as averages
518 instead of individually (Pearce, 2014). Samples display an almost flat pattern
519 subparallel to N-MORB, with a marked negative Nb+Ta anomaly suggesting that they
520 probably formed in a supra-subduction zone setting (Pearce, 2008, 2014). In the Th/Yb
521 versus Nb/Yb diagram of Pearce (2008), most samples show high Th/Nb ratios (Fig.
522 11c) which are typical of basaltic rocks from supra-subduction zones (Pearce, 2014).
523 Th/Yb and Nb/Yb values of 0.02 to 0.47 and 0.21 to 6.40 (Table S5), respectively, for
524 the studied samples span from the limit of the MORB-OIB array to higher Th/Yb ratios
525 towards the oceanic island arc field, with two samples plotting within this field (Fig.
526 11c). The relations between V and Ti also point to a supra- subduction zone setting
527 (Fig. 11d). All samples show low V/Ti and plot in the MORB and slab-distal back-arc
528 basin basalts and fore-arc basalts field (Fig. 11d; $\text{V/Ti} = 0.02$ to 0.04 , Table S5). In
529 sum, the geochemical features of the CMU high-P metamafic rocks indicate a supra-
530 subduction zone setting for their genesis, most likely in a back-arc or forearc basin.
531 This assumption fits well with the existence of a magmatic arc-system in the periphery
532 of Gondwana during the Late Ediacaran to Early Ordovician times, but this hypothesis
533 needs to be confirmed by isotopic dating. This new interpretation contrasts with a
534 previously proposed anorogenic setting where basaltic magmas intruded continental
535 crust (Leal, 2001).

536

537 **6. DISCUSSION**

538 **6.1 Atoll garnet formation**

539 Atoll garnet structures developed close to the metamorphic peak (stage 2, Figs. 6 and
540 7). Several authors (e.g., Cao et al., 2018; Fayard et al., 2010; Hyppolito et al., 2016)
541 proposed that the most likely context for the development of atoll texture is the
542 formation of micro-cracks which serve as pathways for fluid infiltration within garnet.
543 Alternatively, coalescence and multiple nucleation of garnet crystals have been
544 proposed (e.g., Spiess et al., 2001). The existence of microveins in garnet crystals of
545 the Safira eclogites (Fig. 3e,f) supports a fluid infiltration process as responsible of the
546 atoll garnet formation. In this scenario, compositional peninsulas and islands formed
547 due to the replacement of garnet I by garnet II in ‘complete’ garnets. Fayard et al.
548 (2010) have proposed that peninsulas may have played the role of principal channels
549 for fluid infiltration. As an atoll structure evolves, the consumption of garnet I cores
550 release elements which were incorporated into garnet II rings, peninsulas and islands,
551 as well as in other phases contained in the atolls (and the matrix) such as
552 clinopyroxene or amphibole. Higher Mn content of garnet II compared to Mn content in
553 the outermost part of garnet I is evidence for the release of this element upon garnet I
554 dissolution and incorporation into garnet II (Fayard et al., 2010). However, the process
555 involved a large-scale multicomponent reaction in a more complex effective bulk
556 composition, for replacement of garnet I cores included the formation of garnet II (rings
557 around garnet I and fine-grained matrix crystals), glaucophane, phengite, rutile and
558 omphacite.

559

560 **6.2 Metamorphic evolution**

561 Fig. 9a,b shows the PT evolution proposed for the studied eclogite samples of the
562 Cubito-Moura Unit. Both trajectories show a first prograde segment that implies
563 simultaneous burial and heating from initial conditions recorded at ~19-21 kbar at 550-
564 570 °C to ~24-25 kbar (~85-90 km depth), at ~585 °C. The associated thermal gradient
565 yields ~7 °C/km, typical of cold subduction zones. After reaching peak pressure, the

566 rocks (unit) detached from the subducting slab and started exhumation in the
567 subduction channel. The process involved heating, as a likely consequence of arrest of
568 subduction due to stacking of incoming units. The metamorphic peak attained during
569 exhumation reached ~630 °C (at ~19 kbar), and was followed by subsequent near-
570 isothermal decompression down to ~15 kbar (c. 50 km depth), suggesting late tectonic-
571 assisted (likely extension) exhumation of the unit.

572

573 **6.3 Tracking the Late Devonian metamorphic belt across the Iberian Massif and** 574 **other Variscan correlatives**

575 The recent correlation of the Late Devonian metamorphic belt across the Iberian
576 Massif proposed by Díez Fernández and Arenas (2015) has been discussed by
577 Simancas et al. (2016). In NW Iberian Massif, the intermediate-T eclogite facies rocks
578 from the Lower Sequence of the Malpica-Tui Unit record a burial path up to peak
579 pressure of c. 23 kbar at 540-620 °C followed by an almost isothermal decompression
580 (Li and Massone, 2016, 2017; Li et al., 2017; paths 6, 7 and 8 in Fig. 12). The
581 comparison with the Safira eclogites from the Lower Sequence of the CMU shows very
582 similar metamorphic evolution (paths 9 and 10 in Fig. 12). The prograde zonation of
583 garnet in the CMU eclogites yield burial to c. 24-25 kbar at 580-600 °C, similar to that
584 of the Malpica-Tui Unit (Fig. 12), though exhumation of the Safira eclogites was
585 accompanied by heating up to peak 620-630 °C at c. 19-20 kbar, previous to strong
586 decompression.

587

588 The PT conditions reported for the blueschists and glaucophane-bearing
589 eclogites are still poorly constrained in the Alvito-Viana do Alentejo area (CMU),
590 although high-P metamorphism has been dated at c. 370 Ma (Moita et al., 2005). In the
591 Upper Sequence of the BCU, PT conditions of c. 20 kbar and 550 °C were recently
592 reported for the Late Devonian metamorphic peak of high-P metapelites (path 16, Fig.
593 12, Arenas et al., In press). On the other hand, in the Upper Sequence of the Malpica-

594 Tui Complex, the Ceán Unit reached PT conditions of c. 19-22 kbar and 460-520 °C
595 during the Late Devonian metamorphic event (López-Carmona et al., 2010, 2013,
596 2014) (Fig. 12 and 13). Arenas et al. (In press) proposed that the BCU and Ceán units
597 share the same PT evolution related to subduction of the Basal Units. At present, more
598 exhaustive work in the Alvito-Viana do Alentejo high-P, low- to intermediate-T rocks
599 should be accomplished in the future to better constrain their PT evolution in order to
600 confirm correlations with similar rocks of the NW Iberian Massif. However, similarities
601 between the lithostratigraphy of the Basal Units from NW and SW Iberia, structural
602 position in the allochthonous pile, tectonothermal evolution and high-P metamorphic
603 ages seems to fairly support the correlation of both terranes in the Iberian Massif.

604

605 In a larger regional context, the Late Devonian high-P-, low- to intermediate-T
606 metamorphic belt can be followed along the Variscan massifs in Europe (Fig. 1a),
607 where it is overlain by ophiolitic units which, in turn, rest under an Early Devonian high-
608 P, high-T belt (Arenas et al., In press; Ballèvre et al., 2014; Kroner and Romer, 2013;
609 Martínez Catalán et al., 2020). This distribution of Variscan allochthonous units is found
610 in the Bohemian, Armorican and Iberian massifs, where the tectonic units show
611 similarities in the structural position, lithostratigraphy, age of the protoliths and
612 tectonothermal evolution.

613

614 In the northern border of the Bohemian Massif, a discontinuous E-W-trending
615 high-P, low-T belt contains glaucophane-bearing metabasites and micaschists that
616 reached PT peak conditions of 11-20 kbar and 350-550 °C (Fayard and Kachlík, 2013).
617 A correlation between the high-P metamorphic belts of the Bohemian and NW Iberian
618 massifs has been recently proposed by Martínez Catalán et al. (2020). In the
619 Armorican Massif, the Basal Allochthonous Units are well preserved in the
620 Champtoceaux and Essarts Complexes, where they include eclogite-facies metapelites
621 with peak conditions ranging from 15-20 kbar at 550 °C to 20-25 kbar at 650 °C,

622 followed by near-isothermal decompression (Ballèvre and Marchand, 1991). This high-
623 P metamorphic event was dated at c. 356-362 Ma (U-Pb data on zircon and Sm-Nd
624 isochron; Bosse et al., 2000; Maurel et al., 2003). Structurally above, in the Ile-de-Groix
625 and Bois-de-Cené units, blueschists-facies metabasites and micaschists (Ballèvre et
626 al., 2003; Bosse et al., 2002; El Khor et al., 2009) reached peak PT conditions of 16-18
627 kbar and 450-500 °C (Bosse et al., 2002). In these tectonic units, high-P
628 metamorphism is dated at c. 360-370 Ma (Rb-Sr and $^{40}\text{Ar}/^{39}\text{Ar}$ methods). The structural
629 position, lithostratigraphy and tectonothermal evolution of the Basal Allochthonous
630 Units in the Armorican Massif is quite similar to those of the Iberian Massif, which led to
631 the corresponding correlations proposed by Ballèvre et al. (2014) for the European
632 Variscan belt.

633

634 **6.4 Protoliths and geodynamic inferences**

635 Based on the new geochemical results, the protoliths of the eclogites in the
636 CMU were probably generated in a supra-subduction zone setting, likely related to a
637 Cadomian magmatic arc system in the Gondwana margin. The Cadomian magmatic
638 arc was located in the margin of the West African Craton, as indicated by provenance
639 analysis of the Ediacaran sedimentary rocks from SW Iberia and NW Iberia equivalents
640 (Chichorro et al., 2008; Díez Fernández et al., 2010, 2017; Fuenlabrada et al., 2012;
641 Pereira et al., 2008). Felsic and mafic magmas intruded the Ediacaran to Middle
642 Cambrian sedimentary sequences probably deposited in a back-arc or forearc basin. It
643 occurred during the Cambrian in the CMU (Chichorro et al., 2008), and in the
644 Cambrian-Ordovician in the BCU and NW Iberia (Abati et al., 2018; Díez Fernández et
645 al., 2012). These differences in age are attributed to slightly different lateral positions of
646 the Basal Units along the margin of Gondwana combined with diachronic magmatic
647 events (Díez Fernández et al., 2017; Fuenlabrada et al., 2020).

648

649 The earliest interactions between Gondwana and Laurussia continental margins
650 started in the Early Devonian and culminated with the assembly of Pangea (Arenas et
651 al., 2014; Díez Fernández et al., 2016; Franke, 1989, 2000; Kröner and Romer, 2013;
652 Matte, 1991, 2001; Martínez Catalán et al., 1997; Simancas et al., 2005; Ribeiro et al.,
653 2007). In this study, we adopt a geodynamic model in which an intra-Gondwana
654 subduction zone dipping towards Laurussia formed in relation to a lithospheric neck in
655 the peri-Gondwana margin at c. 400-410 Ma (Díez Fernández et al., 2016). This
656 subduction system led to the formation of a first Early Devonian high-P, high-T
657 metamorphic belt, presently preserved in the Upper Allochthonous Units (Fernández-
658 Suárez et al.; 2007; Mendía et al., 2001). Subsequent opening of Middle Devonian
659 ephemeral oceanic basins, due to strike-slip tectonics (pull-apart type; Arenas et al.,
660 2014) or due to extension in the upper plate (suprasubduction type; Díez Fernández et
661 al., 2020), was followed by the simultaneous subduction of the whole Basal Units
662 during Late Devonian times (c. 377-370 Ma, Abati et al., 2010, 2018; Beranoaguirre et
663 al., 2019; Moita et al., 2005). Considering the PT gradient of the Lower Sequence in
664 NW Iberia (paths 1 to 8; Fig. 12; Arenas et al., 1995, 1997; Martínez Catalán et al.,
665 1996), the Safira eclogites from the CMU show a slightly higher P and T at the baric
666 peak conditions (paths 9 and 10, Fig. 12), suggesting a deeper position within the
667 subducting slab. The proposed model for the exhumation of the Basal Allochthonous
668 Units in NW Iberia was accompanied by the development of ductile thrusts that overlain
669 the deepest domains from the Lower Sequence (i.e. Agualada and Espasante units;
670 paths 11 and 12; Fig. 12) over the Upper Sequence, and subsequent development of
671 recumbent folds (Martínez Catalán et al., 1996; Díez Fernández et al., 2011).

672

673 **7. CONCLUSIONS**

674 In the SW Iberian Massif, the Cubito-Moura Unit (CMU) represents a high-P,
675 low- to intermediate-T metamorphic belt. Thermodynamic modelling of intermediate-T
676 eclogites from the Lower Sequence of the CMU in the MnNCKFMASHT system

677 indicates a prograde PT evolution up to ~24 kbar and 585 °C, followed by
678 decompression accompanied by moderate heating (~19 kbar, 630 °C), and a
679 subsequent isothermal decompression to 15 kbar. This evolution suggests deeper
680 subduction of the CMU during the Late Devonian (c. 370 Ma) than previously thought.
681 The CMU shares similar lithostratigraphic sequences and tectonothermal evolution with
682 the Badajoz-Córdoba Unit (BCU), and the Basal Allochthonous Units of NW Iberian
683 Massif. We propose that they represent equivalent allochthonous terranes with a
684 common tectonothermal history since Late Ediacaran to Carboniferous times. The
685 Basal Allochthonous Units in NW and SW Iberian Massif are considered the remnants
686 of an arc-derived section built on the thinned margin of Gondwana during Late
687 Ediacaran-Cambrian times, later subducted during the first stages of the assembly of
688 Pangea. Along the Armorican, Bohemian and Iberian massifs, allochthonous terranes
689 with similar lithostratigraphy and Variscan tectonothermal evolution conform a single
690 Late Devonian high-P, low- to intermediate-T metamorphic belt developed during the
691 amalgamation of Pangea that can be followed along the Variscan Orogen in Europe for
692 thousands of kilometers.

693

694 **ACKNOWLEDGEMENTS**

695 Funding has been provided by the Spanish project CGL2016-76438-P
696 (Ministerio de Economía, Industria y Competitividad) and a FPU pre-doctoral grant to
697 I.N.F. (FPU16/05281, Ministerio de Ciencia, Innovación y Universidades). M.F. Pereira
698 acknowledges financial support by FCT (Portugal): project UIDB/04683/2020- ICT. This
699 paper is a contribution to project IUGS-UNESCO IGCP 683- Pre-Atlantic geological
700 connections among northwest Africa, Iberia and eastern North America: implications for
701 continental configurations and economic resources. We thank the comments of two
702 anonymous reviewers that have contributed to improve the content of this manuscript.

703

704

705 **FIGURE CAPTION**

706

707 Fig. 1. a) Zonation of the Variscan Orogen in Europe (Díez Fernández and Arenas,
708 2015). b) Geological map of the Iberian Massif. In NW Iberia, the Internal Variscan
709 Zone is represented in the allochthonous complexes of Cabo Ortegal (COC),
710 Órdenes (OC), Malpica-Tui (MTC), Bragança (BC) and Morais (MC), whereas in
711 SW Iberia is represented by the Ossa-Morena Complex (OMC). AF, Azuaga Fault;
712 BAO, Beja-Acebúches Ophiolite; CA, Carvalhal Amphibolites; CF, Canaleja Fault;
713 CMU, Cubito-Moura Unit; CO, Calzadilla Ophiolite; BCU, Badajoz-Córdoba Unit;
714 ET, Espina Thrust; HF, Hornachos Fault; IOMZO, Internal Ossa-Morena Zone
715 Ophiolites; LLF, Llanos Fault; MLF, Malpica-Lamego Fault; OF, Onza Fault; OVD,
716 Obejo-Valsequillo Domain; PG-CVD, Puente Génave-Castelo de Vide
717 Detachment; PRF, Palas de Rei Fault; PTF, Porto-Tomar Fault; RF, Riás Fault;
718 VF, Viveiro Fault. After Díez Fernández and Arenas (2015) and Arenas et al.
719 (2016b).

720

721 Fig. 2. a) Geological map of the southern part of the Évora Massif and b) composite
722 cross-section (Díez Fernández et al., 2017). See Fig. 1b for location. c)
723 Tectonostratigraphic column of the Lower Sequence of the Basal Units in the
724 Évora Massif. d) Tectonostratigraphic column of the Carvalhal ophiolite (Díez
725 Fernández et al., 2017). The star indicates the location of the Safira eclogites
726 sampled and studied in this work.

727

728

729 Fig. 3. Microphotographs of the studied eclogites. a) and b) Plane-polarized light (a)
730 and cross-polarized light (b) of eclogite sample 116748. c) and d) Plane-polarized
731 light (c) and cross-polarized light (d) of eclogite sample 116747. e) and f) BSE
732 images showing microveins in sample 116748 (e) and 116747 (f).

733

734 Fig. 4. a) and b) Phase maps constructed after manipulation of X-ray maps showing
735 the distribution of mineral phases in samples 116748 and 116747, respectively. c)
736 X-Ray map showing Ca content (apfu) in garnet (sample 116748). d) X-Ray map
737 showing Mn content (apfu) in garnet (sample 116748). e) X-Ray map of Mg
738 content (apfu) in garnet (sample 116748). f) X-Ray map of Fe content (apfu) in
739 garnet (sample 116748). g) X-Ray map showing Na/(Na+Ca) ratio (counts) in
740 clinopyroxene (sample 116748). The selected area corresponds to a different area
741 to those of c-f. h) X-Ray map showing Ca content (apfu) in garnet (sample
742 116747). i) X-Ray map showing Mn content (apfu) in garnet (sample 116747). j) X-
743 Ray map showing Fe content (apfu) in garnet (sample 116747). k) X-Ray map
744 showing Na/(Na+Ca) ratio (counts) in clinopyroxene (sample 116747). The
745 selected area corresponds to a different area to those of h-j.

746

747 Fig. 5. a) Triangular diagram showing the chemical composition of garnet (Coleman et
748 al., 1965). b) and c) Chemical profile of garnet in samples 116748 (b) and 116747
749 (c). d) Composition of omphacite with indication of the end-members. e) and f)
750 Chemical profile of clinopyroxene in samples 116748 (e) and 116747 (f). g)
751 Composition of phengite with indication of the end-members. h), i) and j)
752 Composition of amphiboles plotted in the classification scheme of Leake et al.
753 (1997).

754

755 Fig. 6. Summary of the observed mineral parageneses in sample 116747 in the
756 framework of metamorphic stages.

757

758 Fig. 7. ACFN phase diagrams for samples 116747 projected from phases quartz, rutile
759 and H₂O fluid and along the exchange vectors MnFe₋₁, MgFe₋₁, and KNa₋₁ (Fe =
760 Fe²⁺_{total}). Red squares correspond to the composition of the end-members of solid

761 solutions of interest. Colored circles represent the measured mineral composition.
762 Diamond corresponds to the bulk composition. a), b) and c) diagrams for
763 metamorphic stages 1, 2 and 3 in sample 116747, respectively.

764

765 Fig. 8. Results of thermodynamic modelling of sample 116747. a) Isochemical phase
766 diagram. The thermodynamic variance increases from lighter to darker color. The
767 main assemblage transitions are marked by colored thick lines. b) Isopleths of Si
768 content in phengite. c) Isopleths of grossular content in garnet. d) Isopleths of
769 pyrope content in garnet. e) Isopleths of almandine content in garnet. f) Isopleths
770 of Al in clinopyroxene. In b)-f), the color scale indicates concentration. Mineral
771 abbreviations are after Whitney and Evans (2010).

772

773 Fig. 9. PT paths proposed for the eclogite samples 116747 (a) and 116748 (b) based
774 on the thermodynamic modelling. In orange, isopleths of volume of garnet (vol. %).

775

776 Fig. 10. Isochemical phase diagrams showing isopleths of volume (%) of a) garnet, b)
777 clinopyroxene, c) amphibole and d) plagioclase.

778

779 Fig. 11. Immobile-element geochemical diagrams of eclogites from the Lower and
780 Upper Sequences (Cubito-Moura Unit). a) Zr/Ti-Nb/Y diagram for the classification
781 of protoliths (Pearce, 1996). b) Incompatible immobile element patterns normalized
782 to N-MORB (Sun and McDonough, 1989). c) Diagram based on the Th-Nb proxy to
783 discriminate mid-ocean ridge and suprasubduction basalts (Pearce, 2014). d)
784 Discrimination diagram based on the V-Ti proxy to distinguish subduction-zone
785 basalts (Pearce, 2014, based on Shervais, 1982).

786

787 Fig. 12. PT diagram showing the PT trajectories proposed for the Basal Units of the
788 Iberian Massif. Location of the rocks is showed in Fig. 13. 1) Basal Forcarei Unit

789 (Órdenes Complex, Martínez Catalán et al., 1996). 2) Middle Forcarei Unit
790 (Órdenes Complex, Martínez Catalán et al., 1996). 3) Upper Forcarei Unit
791 (Órdenes Complex, Martínez Catalán et al., 1996). 4) Lalín Unit (Órdenes
792 Complex, Martínez Catalán et al., 1996). 5) Santiago Unit (Órdenes Complex,
793 Arenas et al., 1995). 6) 7) and 8) Malpica-Tui Unit (Malpica-Tui Complex, Li and
794 Massone, 2016, 2017; Li et al., 2017). 9) CMU (Ossa-Morena Complex, sample
795 116748, this work). 10) CMU (Ossa-Morena Complex, sample 116747, this work).
796 11) Agualada Unit (Órdenes Complex, Arenas et al., 1997). 12) Espasante Unit
797 (Cabo Ortegal Complex, Arenas, 1991). 13), 14) and 15) Ceán Unit (Malpica-Tui
798 Complex, López-Carmona et al., 2010, 2013, 2014). 16) BCU (Ossa-Morena
799 Complex, Arenas et al., In press). In purple the PT path inferred for the mantle
800 wedge located above the accretionary complex (Martínez Catalán et al., 1996).

801

802 Fig. 13. Geological map of the Iberian Massif showing the distribution of high-P rocks
803 from the Basal Units referenced in Fig. 12.

804

805

806 TABLE CAPTION

807 Table 1. Chemical analysis of the studied Safira eclogites (wt.%). The input values for
808 the calculation of the isochemical phase diagrams are also shown (atomic molar
809 proportions).

810

811 SUPPLEMENTARY MATERIAL

812

813 Figure S1. Results of thermodynamic modelling of sample 116748. a) Isochemical
814 phase diagram. The thermodynamic variance increases from lighter to darker
815 color. The main assemblage transitions are marked by colored thick lines. b)
816 Isopleths of Si content in phengite. c) Isopleths of grossular content in garnet. d)

817 Isopleths of pyrope content in garnet. e) Isopleths of almandine content in garnet.
818 f) Isopleths of $\text{Al}_{(\text{M1m})}$ in clinopyroxene. In b)-f), the color scale indicates
819 concentration. Mineral abbreviations are after Whitney and Evans (2010).

820

821 Table S1. Representative chemical analysis of garnet. Analysis marked with an
822 asterisk correspond to the chemical profiles.

823

824 Table S2. Representative chemical analysis of clinopyroxene. Analysis marked with an
825 asterisk correspond to the chemical profiles.

826

827 Table S3. Representative chemical analysis of amphibole.

828

829 Table S4. Representative chemical analysis of white micas and plagioclase.

830

831 Table S5. Whole rock analysis of major (wt%) and trace elements (ppm) from the high-
832 P rocks samples of the Safira and Alvito-Viana do Alentejo areas (CMU).

833

834 tcdb55c2d. Database used in this work.

835

836 THERIN. Input used in this work.

837

838

839

840

841

842

843

844

845 REFERENCES

846

847 Ábalos, B., Gil Ibarguchi, J.I., Eguiluz, L., 1991. Cadomian subduction, collision and
848 Variscan transpression in the Badajoz-Córdoba Shear Belt, southwest Spain.
849 Tectonophysics 199, 51-72.

850

851 Ábalos, B., Puelles, P., Gil Ibarguchi, J.I., 2003. Structural assemblage of high-
852 pressure mantle and crustal rocks in a subduction channel (Cabo Ortegal, NW
853 Spain). Tectonics 22, 1-21.

854

855 Abati, J., Gerdes, A., Fernández Suárez, J., Arenas, R., Whitehouse, M.J., Díez
856 Fernández, R., 2010. Magmatism and early-Variscan continental subduction in the
857 northern Gondwana margin recorded in zircons from the basal units of Galicia, NW
858 Spain. Geological Society of America Bulletin 122, 219-235.

859

860 Abati, J., Arenas, R., Díez Fernández, R., Albert, R., Gerdes, A., 2018. Combined
861 zircón U-Pb and Lu-Hf isotopes study of magmatism and high-P metamorphism of
862 the basal allochthonous units in the SW Iberian Massif (Ossa-Morena Complex).
863 Lithos 322, 20-37.

864

865 Andonaegui, P., Abati, J., Díez Fernández, R., 2017. Late Cambrian magmatic arc
866 activity in peri-Gondwana: geochemical evidence from the Basal Allochthonous
867 Units of NW Iberia. Geologica Acta 15(4): 305-321.

868

869 Arenas, R., 1991. Opposite P, T, t paths of Hercynian metamorphism between the
870 upper units of the Cabo Ortegal Complex and their substratum (northwest of the
871 Iberian Massif). Tectonophysics 191, 347-364.

872

- 873 Arenas, R., Sánchez Martínez, S., 2015. Variscan ophiolites in NW Iberia: tracking lost
874 Paleozoic oceans and the assembly of Pangea. *Episodes* 38, 315–333.
- 875
- 876 Arenas, R., Rubio Pascual, F.J., Díaz García, F., Martínez Catalán, J.R., 1995. High-
877 pressure microinclusions and development of an inverted metamorphic gradient in
878 the Santiago schists (Órdenes Complex, NW Iberian Massif, Spain): evidence of
879 subduction and syn-collisional decompression. *Journal of Metamorphic Geology* 13,
880 141-164.
- 881
- 882 Arenas, R., Abati, J., Martínez Catalán, J.R., Díaz García, F., Rubio Pascual, F.J.,
883 1997. P-T evolution of eclogites from the Agualada Unit (Órdenes Complex,
884 northwest Iberian Massif, Spain): Implications for crustal subduction. *Lithos* 40, 221-
885 242.
- 886
- 887 Arenas, R., Díez Fernández, R., Sánchez Martínez, S., Gerdes, A., Fernández-Suárez,
888 J., Albert, R., 2014. Two-stage collision: Exploring the birth of Pangea in the
889 Variscan terranes. *Gondwana Research* 25, 756-763.
- 890
- 891 Arenas, R., Sánchez Martínez, S., Díez Fernández, R., Gerdes, A., Abati, J.,
892 Fernández-Suárez, J., Andonaegui, P., González Cuadra, P., López Carmona, A.,
893 Albert, R., Fuenlabrada, J.M., Rubio Pascual, F.J., 2016a. Allochthonous terranes
894 involved in the Variscan suture of NW Iberia: A review of their origin and
895 tectonothermal evolution. *Earth-Science Reviews* 161, 140-178.
- 896
- 897 Arenas, R., Díez Fernández, R., Rubio Pascual, F.J., Sánchez Martínez, S., Martín
898 Parra, L.M., Matas, J., González del Tánago, J., Jiménez-Díaz, A., Fuenlabrada,
899 J.M., Andonaegui, P., Garcia-Casco, A., 2016b. The Galicia-Ossa-Morena Zone:

- 900 Proposal for a new zone of the Iberian Massif. Variscan implications.
901 Tectonophysics 681, 135-143.
- 902
- 903 Arenas, R., Novo-Fernández, I., García-Casco, A., Díez Fernández, R., Fuenlabrada,
904 J.M., Pereira, M.F., Abati, J., Sánchez Martínez, S., Rubio Pascual, F.J., In press. A
905 unique blueschist facies metapelite with Mg-rich chloritoid from the Badajoz-
906 Córdoba Unit (SW Iberian Massif): Correlation of Late Devonian high-pressure belts
907 along the Variscan Orogen. International Geology Review.
908 <https://doi.org/10.1080/00206814.2020.1789509>
- 909
- 910 Azor, A., Lodeiro, F.G., Simancas, J.F., 1994. Tectonic evolution of the boundary
911 between the Central Iberian and the Ossa-Morena zones (Variscan belt, southwest
912 Spain). Tectonics 13, 45-61.
- 913
- 914 Baldwin, J.A., Powell, R., Brown, M., Moraes, R., Fuck, R.A., 2005. Modelling of
915 mineral equilibria in ultrahigh-temperature metamorphic rocks from the Anapolis-
916 Itaucu Complex, central Brazil. Journal of Metamorphic Geology 23, 511-531.
- 917
- 918 Ballèvre, M., Marchand, J., 1991. Zonation du métamorphisme éclogitique dans la
919 nappe de Champtoceaux (Massif armoricain, France). Comptes-Rendus de
920 l'Académie des Sciences de Paris, Serie II (312), 705-711.
- 921
- 922 Ballèvre, M., Pitra, P., Bohn, M., 2003. Lawsonite growth in the epidote blueschists
923 from the Ile de Groix (Armorican Massif, France): a potential geobarometer. Journal
924 of Metamorphic Geology 21, 723-735.
- 925
- 926 Ballèvre, M., Martínez Catalán, J.R., López-Carmona, A., Abati, J., Díez Fernández,
927 R., Ducassou, C., Pitra, P., Arenas, R., Bosse, V., Castiñeiras, P., Fernández-

- 928 Suárez, J., Gómez Barreiro, J., Paquette, J.-L., Poujol, M., Ruffet, G., Sánchez
929 Martínez, S., 2014. Correlation of the nappe stack in the Ibero-Armorican arc across
930 the Bay of Biscay: a joint French-Spanish project, in: Schulmann, K., Martínez
931 Catalán, J.R., Lardeaux, J.M., Oggiano, G. (eds.), *The Variscan Orogeny: Extent,*
932 *Timescale and the Formation of the European Crust*. Geological Society, London,
933 Special Publications 405, 77-113.
- 934
- 935 Bence, A.E., Albee, A.L., 1968. Empirical correction factors for the electron
936 microanalysis of silicates and oxides. *Journal of Geology* 76, 382–403.
- 937
- 938 Beranoaguirre, A., Puelles, P., Ábalos, B., Gil Ibarguchi, J.I., García de Madinabeitia,
939 S., 2019. Short-duration regional metamorphic event recorded in a Variscan
940 subduction channel (Malpica-Tui eclogites, NW Iberia). *International Journal of Earth
941 Sciences* 108, 2037-2046.
- 942
- 943 Bosse, V., Féraud, G., Ruffet, G., Ballèvre, M., Peucat, J.-J., De Jong, K., 2000. Late
944 Devonian subduction and early orogenic exhumation of eclogite-facies rocks from
945 the Champtoceaux complex (Variscan belt, France). *Geological Journal* 35, 297-
946 325.
- 947
- 948 Bosse, V., Ballèvre, M., Vidal, O., 2002. Ductile thrusting recorded by the garnet isograd
949 from blueschist-facies metapelites of the Ile de Groix, Armorican Massif, France.
950 *Journal of Petrology* 43, 485-510.
- 951 Cao, D., Cheng, H., Zhang, L., Wang, K., 2018. Origin of atoll garnets in ultra-high-
952 pressure eclogites and implications for infiltration of external fluids. *Journal of Asian
953 Earth Sciences* 160, 224-238.
- 954

- 955 Carvalhosa, A., Zbyszewski, G., 1994. Carta Geológica de Portugal, Noticia Explicativa
956 da Folha 35-D (Montemor-o-Novo), scale 1:50000. Instituto Geológico e Mineiro
957 (Portugal)
- 958
- 959 Chichorro, M., 2006. Tectonic evolution of Montemor-o-Novo Shear Zone (SW Ossa-
960 Morena Zone – Santiago do Escoural – Cabrela Área). PhD Thesis, Universidade
961 de Évora, Évora, Portugal, 569 pp.
- 962
- 963 Chichorro, M., Pereira, F.M., Díaz-Azpiroz, M., Williams, I.S., Fernández, C., Pin, C.,
964 Silva, J.B., 2008. Cambrian ensialic rift-related magmatism in the Ossa-Morena
965 Zone (Évora-Aracena metamorphic belt, SW Iberian Massif): Sm-Nd isotopes and
966 SHRIMP zircon U-Th-Pb geochronology. *Tectonophysics* 461, 91-113.
- 967
- 968 Coggon, R., Holland, T.J.B., 2002. Mixing properties of phengitic micas and revised
969 garnet-phengite thermobarometers. *Journal of Metamorphic Geology* 20, 683-696.
- 970
- 971 De Capitani, C., Brown, T.H., 1987. The computation of chemical equilibrium in
972 complex systems containing non-ideal solutions. *Geochimica et Cosmochimica Acta*
973 5, 2639-2652.
- 974
- 975 De Capitani, C., Petrakakis, K., 2010. The computation of equilibrium assemblage
976 diagrams with Theriak/Domino software. *American Mineralogist* 95, 1006-1016.
- 977
- 978 Dewey, J., 1975. Plate tectonics. *Reviews of Geophysics* 13, 326-332.
- 979
- 980 Diener, J.F.A., Powell, R., White, R.W., Holland, T.J.B., 2007. A new thermodynamic
981 model for clino- and orthoamphiboles in the system Na₂O-CaO-FeO-MgO-Al₂O₃-
982 SiO₂-H₂O-O. *Journal of Metamorphic Geology* 25, 631-656.

- 983
- 984 Dias da Silva, I., Pereira, M.F., Silva, J.B., Gama, C., 2018. Time-space distribution of
985 silicic plutonism in a gneiss dome of the Iberian Variscan Belt: The Évora Massif
986 (Ossa-Morena Zone, Portugal). *Tectonophysics* 747-748, 298-317.
- 987
- 988 Díez Fernández, R., Martínez Catalán, J.R., Gerdes, A., Abati, J., Arenas, R.,
989 Fernández-Suárez, J., 2010. U-Pb ages of detrital zircons from the Basal
990 allochthonous units of NW Iberia: Provenance and paleoposition on the northern
991 margin of Gondwana during the Neoproterozoic and Paleozoic. *Gondwana*
992 *Research* 18, 385-399.
- 993
- 994 Díez Fernández, R., Martínez Catalán, J.R., Arenas, R., Abati, J., 2011. Tectonic
995 evolution of a continental subduction-exhumation channel: Variscan structure of the
996 basal allochthonous units in NW Spain. *Tectonics* 30, 1-22.
- 997
- 998 Díez Fernández, R., Castiñeiras, P., Gómez Barreiro, J., 2012a. Age constraints on
999 Lower Paleozoic convection system: magmatic events in the NW Iberian
1000 Gondwanan margin. *Gondwana Research* 21, 1066-1079.
- 1001
- 1002 Díez Fernández, R., Martínez Catalán, J.R., Arenas, R., Abati, J., 2012b. The onset of
1003 the assembly of Pangaea in NW Iberia: Constraints on the kinematics of continental
1004 subduction. *Gondwana Research* 22, 20-25.
- 1005
- 1006 Díez Fernández, R., Foster, D.A., Gómez Barreiro, J., Alonso-García, M., 2013.
1007 Rheological control on the tectonic evolution of a continental suture zone: the
1008 Variscan example from NW Iberia (Spain). *International Journal of Earth Sciences*
1009 102, 1305-1319.
- 1010

- 1011 Díez Fernández, R., Arenas, R., 2015. The Late Devonian Variscan suture of the
1012 Iberian Massif: A correlation of high-pressure belts in NW and SW Iberia.
1013 Tectonophysics 654, 96-100.
- 1014
- 1015 Díez Fernández, R., Arenas, R., Francisco Pereira, F., Sánchez-Martínez, S., Albert,
1016 R., Martín Parra, L.M., Rubio Pascual, F.J., Matas, J., 2016. Tectonic evolution of
1017 Variscan Iberia: Gondwana-Laurussia collision revisited. Earth-Science Reviews
1018 162, 269-292.
- 1019
- 1020 Díez Fernández, R., Fuenlabrada, J.M., Chichorro, M., Pereira, M.F., Sánchez-
1021 Martínez, S., Silva, J.B., Arenas, R., 2017. Geochemistry and tectonostratigraphy of
1022 the basal allochthonous units of SW Iberia (Évora Massif, Portugal): Keys to the
1023 reconstruction of pre-Pangean paleogeography in southern Europe. Lithos 268, 285-
1024 301.
- 1025
- 1026 Díez Fernández, R., Arenas, R., Sánchez Martínez, S., Novo-Fernández, I., Albert, R.,
1027 2020. Single subduction zone for the generation of Devonian ophiolites and high-P
1028 metamorphic belts of the Variscan Orogen (NW Iberia). Terra Nova 32, 239-245.
- 1029
- 1030 El Khor, A., Schmidt, S.T., Ballèvre, M., Ulianov, A., Bruguier, O., 2012. Trace element
1031 partitioning in HP-LT metamorphic assemblages during subduction-related
1032 metamorphism, Ile de Groix, France: a detailed LA-ICP-MS U-Pb geochronology of
1033 its Ordovician protolith. International Journal of Earth Sciences 101, 1169-1190.
- 1034
- 1035 Fayard, S.W., Klárová, H., Nosál, L., 2010. Mechanism of formation of atoll garnet
1036 during high-pressure metamorphism. Mineralogical Magazine 74, 111-126.
- 1037

- 1038 Fayard, S.W., Kachlík, V., 2013. New evidence of blueschist facies rocks and their
1039 geotectonic implication for Variscan suture(s) in the Bohemian Massif. *Journal of*
1040 *Metamorphic Geology* 31, 63-82.
- 1041
- 1042 Fernández-Suárez, J., Arenas, R., Abati, J., Martínez Catalán, J.R., Whitehouse, M.J.,
1043 Jeffries, T.E., 2007. U-Pb chronometry of polymetamorphic high-pressure granulites:
1044 an example from the allochthonous terranes of the NW Iberian Variscan belt. In:
1045 Hatcher, R.D., Carlson, M.P., McBride, J.H. and Martínez-Catalán, J.R. (eds.), 4-D
1046 Framework of Continental Crust. Geological Society of America Memoir 200, 469–
1047 488.
- 1048
- 1049 Fonseca, P., Araújo, A., Leal, N., Munhá, J.M., 1993. Variscan glaucophane eclogites
1050 in the Ossa-Morena Zone. XII Reunião de Geologia do Oeste Peninsular (Évora).
1051 Terra Abstracts, supplement n.6 to Terra Nova 5, 11-12.
- 1052
- 1053 Fonseca, P., Munhá, J., Pedro, J., Rosas, F., Moita, P., Araújo, A., Leal, N., 1999.
1054 Variscan ophiolites and high-pressure metamorphism in southern Iberia. *Ophioliti* 24,
1055 259-268.
- 1056
- 1057 Franke, W., 1989. Tectonostratigraphic units in the Variscan belt of central Europe, in:
1058 Dallmeyer, R.D. (ed.), *Terranes in the Circum-Atlantic Paleozoic Orogens*.
1059 Geological Society of America Special Paper 230, 67-90.
- 1060
- 1061 Franke, W., 2000. The mid-European segment of the Variscides: tectonostratigraphic
1062 units, terrane boundaries and plate tectonic evolution. In: Franke, W., Haak, V.,
1063 Oncken, O. and Tanner, D. (eds.), *Orogenic processes: quantification and modelling*
1064 in the Variscan Belt. Geological Society London, Special Publications 179, 35–61.
- 1065

- 1066 Fuenlabrada, J.M., Arenas, R., Sánchez Martínez, S., Díaz García, F., Castiñeiras, P.,
1067 2010. A peri-Gondwana arc in NW Iberia. I: Isotopic and geochemical constraints on
1068 the origin of the arc - A sedimentary approach. *Gondwana Research* 17, 338-351.
- 1069
- 1070 Fuenlabrada, J.M., Arenas, R., Díez Fernández, R., Sánchez Martínez, S., Abati, J.,
1071 López-Carmona, A., 2012. Sm-Nd isotope geochemistry and tectonic setting of the
1072 metasedimentary rocks from the basal allochthonous units of NW Iberia (Variscan
1073 suture, Galicia). *Lithos* 148, 196-208.
- 1074
- 1075 Fuenlabrada, J.M., Arenas, R., Sánchez Martínez, S., Díez Fernández, R., Pieren,
1076 A.P., Pereira, M.F., Chichorro, M., Silva, J.B., 2020. Geochemical and isotopic (Sm-
1077 Nd) provenance of Ediacaran-Cambrian metasedimentary series from the Iberian
1078 Massif. Paleoreconstruction of the North Gondwana margin. *Earth-Science Reviews*
1079 201. In press.
- 1080
- 1081 Garcia-Casco, A., 2007. Magmatic paragonite in trondhjemites from the Sierra del
1082 Convento mélange, Cuba. *American Mineralogist* 92, 1232-1237.
- 1083
- 1084 Garcia-Casco, A., Knippenberg, S., Rodríguez Ramos, R., Harlow, G.E., Hofman, C.,
1085 Pomo, J.C., Blanco-Quintero, I.F., 2013. Pre-Columbian jadeitite artifacts from the
1086 Golden Rock Site, St. Eustatius, Lesser Antilles, with special reference to jadeitite
1087 artifacts from Elliot's, Antigua: Implications for potential source regions and long-
1088 distance exchange networks in the Greater Caribbean. *Journal of Archaeological
1089 Science* 40, 3153–3169.
- 1090
- 1091 Gil Ibarguchi, J.I., Ortega Gironés, E., 1985. Petrology, structure and geotectonic
1092 implications of glaucophane-bearing eclogites and related rocks from the Malpica-
1093 Tuy (MT) unit, Galicia, Northwest Spain. *Chemical Geology* 50, 145-162.

- 1094
- 1095 Gil Ibarguchi, J.I., Mendoza, M., Girardeau, J., Peucat, J.J., 1990. Petrology of eclogites
1096 and clynopyroxene-garnet metabasites from the Cabo Ortegal Complex
1097 (northwestern Spain). *Lithos* 25, 133-162.
- 1098
- 1099 Gil Ibarguchi, J.I., 1995. Petrology of jadeite-metagranite and associated orthogneiss
1100 from the Malpica-Tuy allochthon (Northwest Spain). *European Journal of Mineralogy*
1101 7, 403-415.
- 1102
- 1103 Green, E.C.R., Holland, T.J.B., Powell, R., 2007. An order-disorder model for
1104 omphacitic pyroxenes in the system jadeite-diopside-hedenbergite-acmite, with
1105 applications to eclogite rocks. *American Mineralogist* 92, 1181-1189.
- 1106
- 1107 Holland, T.J.B., Powell, R., 1998. An internally consistent thermodynamic dataset for
1108 phases of petrological interest. *Journal of Metamorphic Geology* 16, 309-343.
- 1109
- 1110 Hyppolito, T., Angiboust, S., Juliani, C., Glodny, J., Garcia-Casco, A., Calderón, M.,
1111 Chopin, C., 2016. Eclogite-, amphibolite- and blueschist-facies rocks from Diego de
1112 Almagro Island (Patagonia): Episodic accretion and thermal evolution of the Chilean
1113 subduction interface during the Cretaceous. *Lithos* 264, 422-440.
- 1114
- 1115 Kato, T., 2005. New accurate Bence-Albee α -factors for oxides and silicates calculated
1116 from the PAP correction procedure. *Geostandards and Geoanalytical Research* 29,
1117 83-94.
- 1118
- 1119 Kroner, U., Romer, R.L., 2013. Two plates - Many subduction zones: The Variscan
1120 orogeny reconsidered. *Gondwana Research* 24, 298-329.
- 1121

- 1122 Leal, N., 2001. Estudo petrológico e geoquímico de rochas metamórficas máficas de
1123 alta pressão das regiões de Alvito-Viana do Alentejo e de Safira (Zona de Ossa-
1124 Morena, Maciço Ibérico). PhD thesis, Universidade de Lisboa, 400pp.
- 1125
- 1126 Leake, B.E., Wooley, A.R., Arps, C.E.S., Birch, W.D., Gilbert, M.C., Grice, J.D.,
1127 Hawthorne, F.C., Kato, A., Kisch, H.J., Krivovichev, V.G., Linthout, K., Laird, J.,
1128 Mandarino, J.A., Maresch, W.V., Nickel, E.H., Rock, N.M.S., Schumacher, J.C.,
1129 Smith, D.C., Stephenson, N.C.N., Ungaretti, L., Whittaker, E.J.W., Youzhi, G., 1997.
1130 Nomenclature of amphiboles: Report of the Subcommittee on Amphiboles of the
1131 International Mineralogical Association, Commission on New Minerals and Mineral
1132 Names. American Mineralogist 82, 1019-1037.
- 1133
- 1134 Li, B., Massone, H-J., 2016. Early Variscan P-T evolution of an eclogite body and
1135 adjacent orthogneiss from the northern Malpica-Tuy shear-zone in NW Spain.
1136 European Journal of Mineralogy 28, 1131-1154.
- 1137
- 1138 Li, B., Massone, H-J., 2017. Contrasting metamorphic evolution of metapelites from the
1139 Malpica-Tuy unit and the underlying so-called parautochthon at the coast of NW
1140 Spain. Lithos 286-287, 92-108.
- 1141
- 1142 Li, B., Massone, H-J., Opitz, J., 2017. Clockwise and Anticlockwise P-T paths of high-
1143 pressure rocks from the 'La Pioza' Eclogite Body of the Malpica-Tuy Complex, NW
1144 Spain. Journal of Petrology 58(7), 1363-1392.
- 1145
- 1146 Lima, S.M., Corfu, F., Neiva, A.M.R., Ramos, J.M.F., 2012. Dissecting Complex
1147 Magmatic Processes: an in-depth U-Pb study of the Pavia Pluton, Ossa-Morena
1148 Zone, Portugal. Journal of Petrology 53, 1887-1911.
- 1149

- 1150 López-Carmona, A., Abati, J., Reche, J., 2010. Petrologic modeling of chloritoid-
1151 glaucophane schists from the NW Iberian Massif. *Gondwana Research* 17, 377-391.
- 1152
- 1153 López-Carmona, A., Pitra, P., Abati, J., 2013. Blueschist-facies metapelites from the
1154 Malpica-Tui Unit (NW Iberian Massif): phase equilibria modelling and H₂O and
1155 Fe₂O₃ influence in high-pressure assemblages. *Journal of Metamorphic Geology*
1156 31, 263-280.
- 1157
- 1158 López-Carmona, A., Abati, J., Pitra, P., Lee, J.K.Q., 2014. Retrogressed lawsonite
1159 blueschists from the NW Iberian Massif: P-T-t constraints from thermodynamic
1160 modelling and ⁴⁰Ar/³⁹Ar geochronology. *Contributions to Mineralogy and Petrology*
1161 167(3), 1-20.
- 1162
- 1163 López Sánchez-Vizcaíno, V., Gómez-Pugnaire, M.T., Azor, A., Fernández-Soler, J.M.,
1164 2003. Phase diagram sections applied to amphibolites: a case study from the Ossa-
1165 Morena/Central Iberian Variscan suture (Southwestern Iberian Massif). *Lithos* 68, 1-
1166 21.
- 1167
- 1168 Martínez Catalán, J.R., Arenas, R., Díaz García, F., Rubio Pascual, F.J., Abati, J.,
1169 Marquínez, J., 1996. Variscan exhumation of a subducted Paleozoic continental
1170 margin: The basal units of the Órdenes Complex, Galicia, NW Spain. *Tectonics* 15,
1171 106–121.
- 1172
- 1173 Martínez Catalán, J.R., Arenas, R., Díaz García, F., Abati, J., 1997. Variscan
1174 accretionary complex of northwest Iberia: terrane correlation and succession of
1175 tectonothermal events. *Geology* 25, 1103–1106.
- 1176

- 1177 Martínez Catalán, J.R., Arenas, R., Abati, J., Sánchez Martínez, S., Díaz García, F.,
1178 Fernández-Suárez, J., González Cuadra, P., Castiñeiras, P., Gómez Barreiro, J.,
1179 Díez Montes, A., González Clavijo, E., Rubio Pascual, F.J., Andonaegui, P., Jeffries,
1180 T.E., Alcock, J.E., Díez Fernández, R., López Carmona, A., 2009. A rootless suture
1181 and the loss of the roots of a mountain chain: The Variscan belt of NW Iberia.
1182 Comptes Rendus Geoscience 341, 114-126.
- 1183
- 1184 Martínez Catalán, J.R., Collett, S., Schulmann, K., Aleksandrowski, P., Mazur, S.,
1185 2020. Correlation of allochthonous terranes and major tectonostratigraphic domains
1186 between NW Iberia and the Bohemian Massif, European Variscan belt. International
1187 Journal of Earth Sciences 109, 1105-1131.
- 1188
- 1189 Mata, J., Munhá, J.M., 1986. Geodynamic significance of high-grade metamorphic
1190 rocks from Degolados-Campo Maior (Tomar-Badajo-Córdoba shear zone). Maleo 2,
1191 28.
- 1192
- 1193 Matte, Ph., 1991. Accretionary history and crustal evolution of the Variscan belt in
1194 Western Europe. Tectonophysics 196, 309–337.
- 1195
- 1196 Matte, Ph., 2001. The Variscan collage and orogeny (480-290Ma) and the tectonic
1197 definition of the Armorica microplate: a review. Terra Nova 13, 122–128.
- 1198
- 1199 Mendía, M., Gil Ibarguchi, J.I., Ábalos, B., 2001. Metamorphic evolution P-T-d-t and
1200 geodynamic meaning of the eclogitic unit of the Cabo Ortegal Complex (NW Spain).
1201 Cadernos Laboratorio Xeolóxico de Laxe 26, 155-178.
- 1202
- 1203 Miyashiro, A., 1973. Paired and unpaired metamorphic belts. Tectonophysics 17, 241-
1204 254.

- 1205
- 1206 Moita, P., 1997. Caracterização petrográfica e geoquímica do metamorfismo de alta
1207 pressão no sector de Viana do Alentejo-Alvito (Zona de Ossa-Morena).
1208 Universidade de Lisboa, MSc thesis, 158 pp.
- 1209
- 1210 Moita, P., Munhá, J., Fonseca, P.E., Pedro, J., Tassinari, C.C.G, Araujo, A., Palácios,
1211 T., 2005. Phase equilibria and geochronology of Ossa Morena eclogites. Actas do
1212 XIV Semana de Gequímina/VIII Congresso de geoquímica dos Países de Língua
1213 Portuguesa 2, 471- 474.
- 1214
- 1215 Moita, P., Santos, J.F., Pereira, F.M., 2009. Layered granitoids: Interaction between
1216 continental crust recycling processes and mantle-derived magmatism.
1217 Examples from the Évora Massif (Ossa-Morena Zone, southwest Iberia,
1218 Portugal). Lithos 111, 125-141.
- 1219
- 1220 Moita, P., Santos, J.F., Pereira, M.F., Costa, M.M., Corfu, F., 2015. The quartz-dioritic
1221 Hospitais intrusión (SW Iberian Massif) and its mafic microgranular enclaves –
1222 Evidence for mineral clustering. Lithos 224-225, 78-100.
- 1223
- 1224 Montero, P., Bea, F., Corretgé, L.G., Floor, P., Whitehouse, M.J., 2009. U-Pb ion
1225 microprobe dating and Sr and Nd isotope geology of the Galiñeiro Igneous
1226 Complex: A model for the peraluminous/peralkaline duality of the Cambro-
1227 Ordovician magmatism of Iberia. Lithos 107, 227-237.
- 1228
- 1229 Morimoto, N., 1988. Nomenclature of pyroxenes. Mineralogical Magazine, 52, 535-550.
- 1230

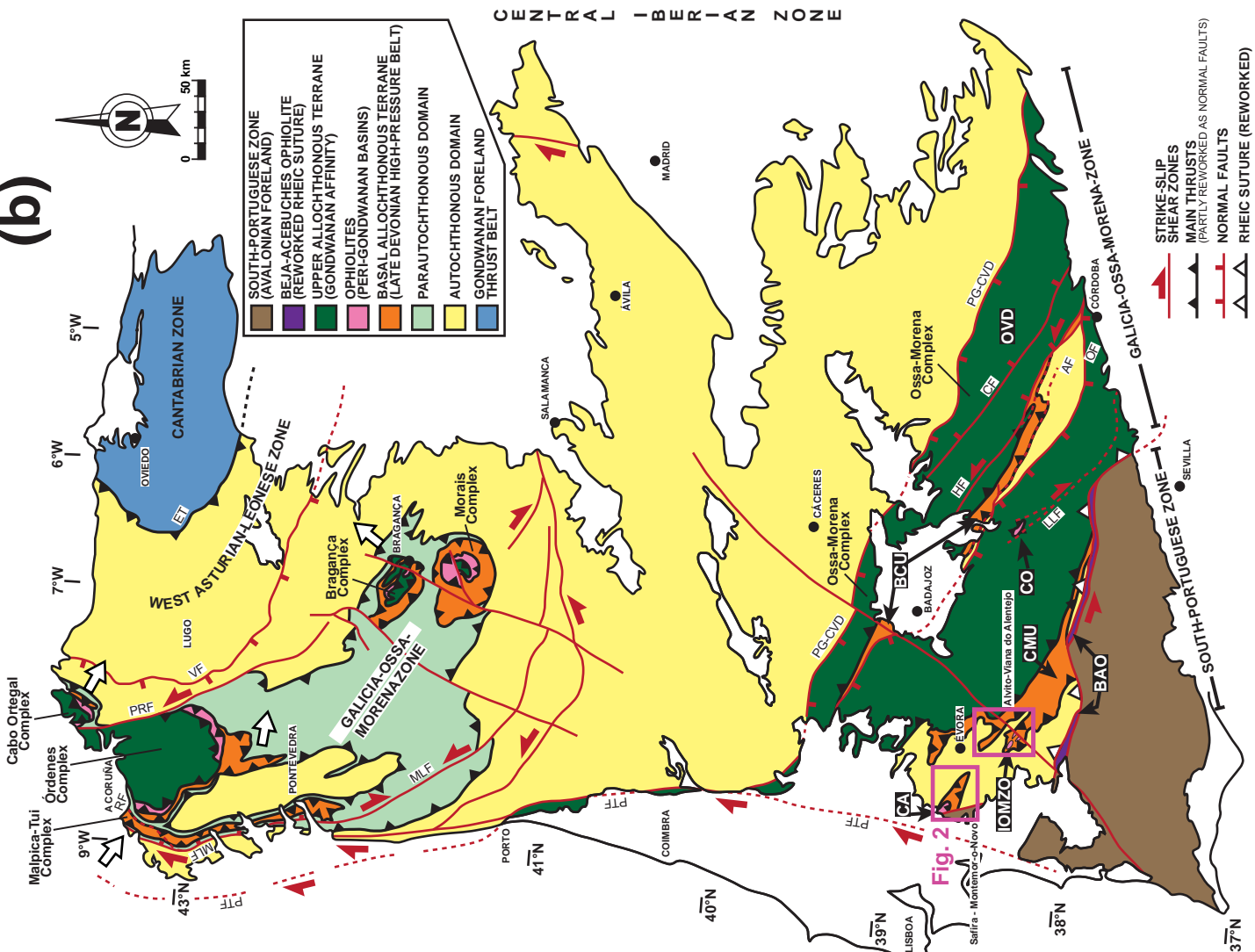
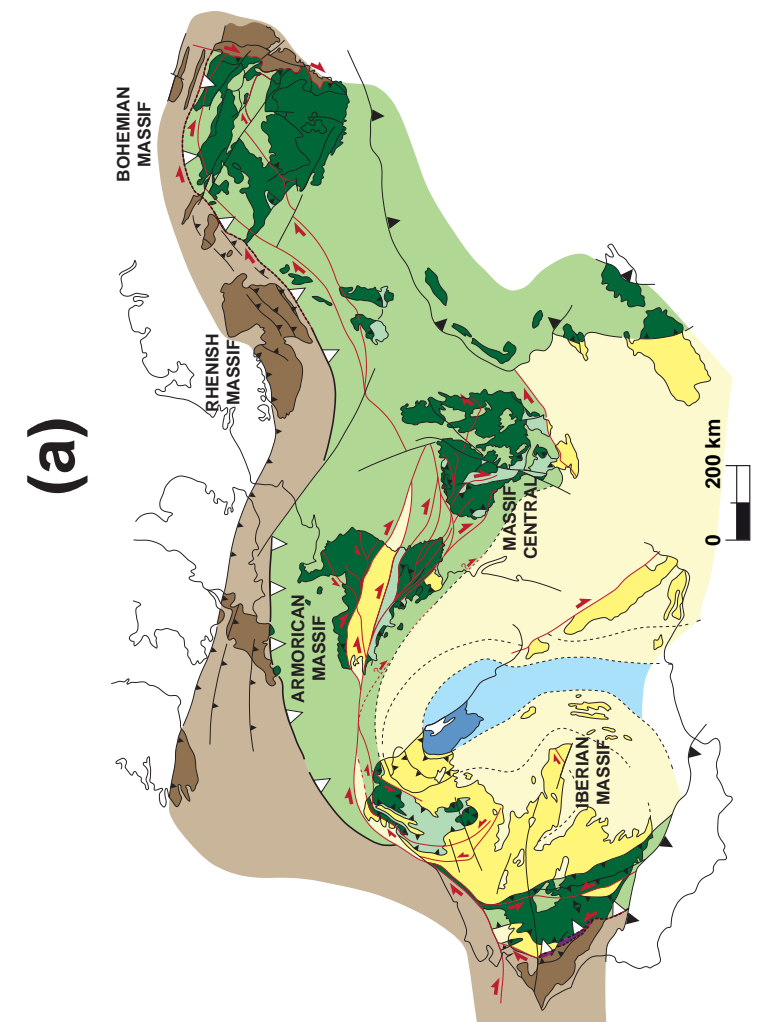
- 1231 Munhá, J.M., Ribeiro, A., Ribeiro, M.L., 1984. Blueschists in the Iberian Variscan Chain
1232 (Tras-os-Montes, NE Portugal). Comunicações dos Serviços Geológicos de
1233 Portugal 70, 31-53.
- 1234
- 1235 Ordóñez-Casado, B., Gebauer, D., Schäfer, H.J., Gil Ibarguchi, J.I., Peucat, J.J., 2001.
1236 A single Devonian subduction event for the HP/HT metamorphism of the Cabo
1237 Ortegal complex within the Iberian Massif. Tectonophysics 332, 359–385.
- 1238
- 1239 Pearce, J.A., 1996. A user's guide to basalt discrimination diagrams. Geological
1240 Association of Canada Special Publication 12, 79-113.
- 1241
- 1242 Pearce, J.A., 2008. Geochemical fingerprinting of oceanic basalts with applications to
1243 ophiolite classification and the search for Archean oceanic crust. Lithos 100, 14-48.
- 1244
- 1245 Pearce, J.A., 2014. Immobile Element Fingerprinting of Ophiolites. Elements 10, 101-
1246 108.
- 1247
- 1248 Pedro, J., 1996. Estudo do metamorfismo de alta pressão na área de Safira
1249 (Montemor-o-Novo) Zona de Ossa-Morena. D.G.F.C.U.L., MSc thesis, 69 pp.
- 1250
- 1251 Pereira, M.F., Silva, J.B., Chichorro, M., Moita, P., Santos, J.F., Apraiz, A., Ribeiro, C.,
1252 2007. Crustal growth and deformational processes in the northern Gondwana
1253 margin: Constraints from the Évora Massif (Ossa-Morena zone, southwest Iberia,
1254 Portugal). In: Linnemann, U., Nance, R.D., Kraft, P. and Zulauf, G. (eds.), The
1255 evolution of Rheic Ocean: From Avalonian-Cadomian active margin to Alleghenian-
1256 Variscan collision. Geological Society of America Special Paper 423, 333-358.
- 1257

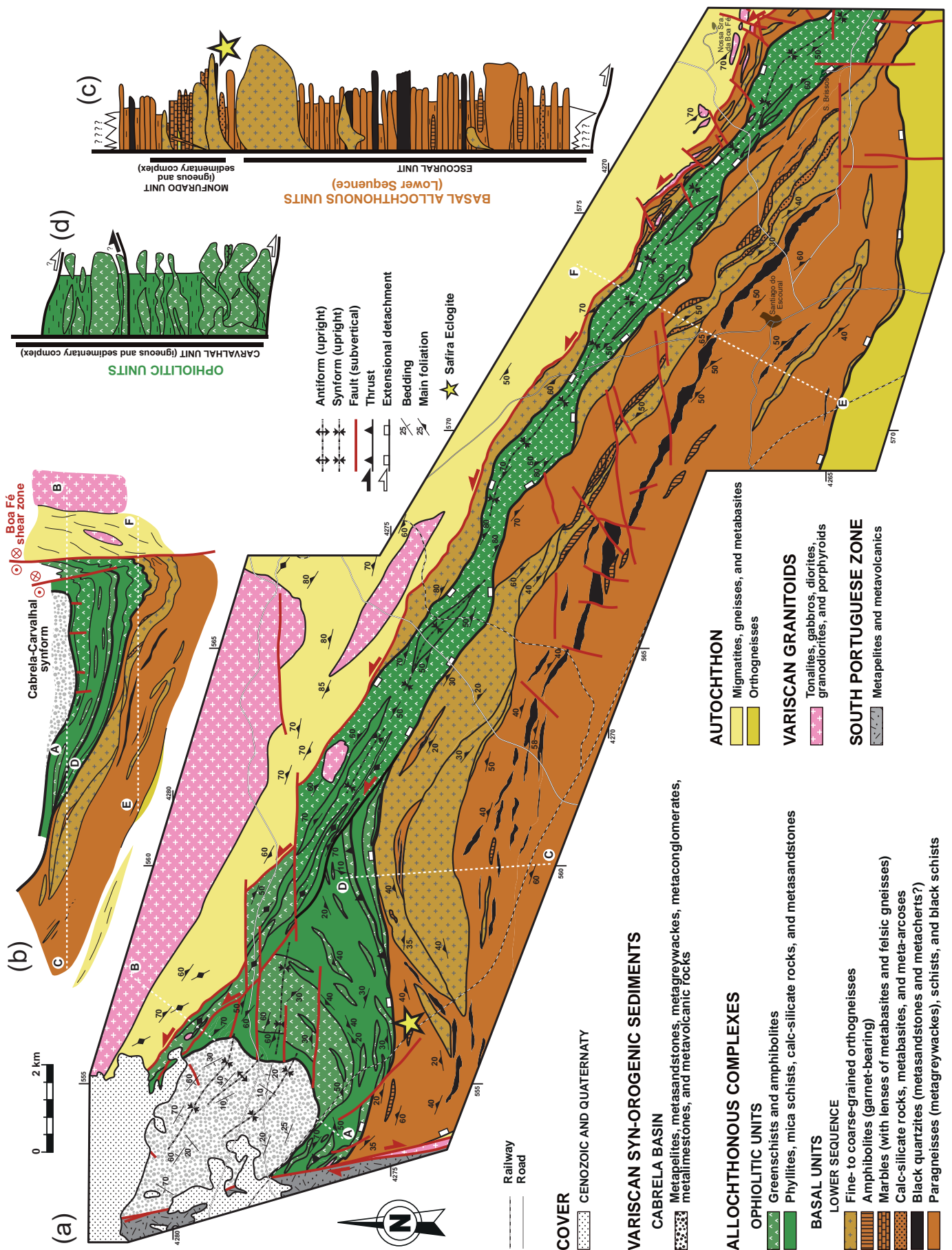
- 1258 Pereira, M.F., Chichorro, M., Williams, I.S., Silva, J.B., 2008. Zircon U-Pb
1259 geochronology of paragneisses and biotite granites from the SW Iberian Massif
1260 (Portugal): evidence for a palaeogeographical link between the Ossa Morena
1261 Ediacaran basins and the West African craton. In: Enninh, N. and Liégeois, J.P.
1262 (eds), The boundaries of the West African Craton. Geological Society of London,
1263 Special Publications 297, 385-408.
- 1264
- 1265 Pereira, M.F., Chichorro, M., Williams, I.S., Silva, J.B., Fernández, C., Díaz-Azpíroz,
1266 M., Apraiz, A., Castro, A., 2009. Variscan intra-orogenic extensional tectonics in the
1267 Ossa-Morena Zone (Évora-Aracena-Lora del Río metamorphic belt, SW Iberian
1268 Massif): SHRIMP zircon U-Th-Pb geochronology. In: Murphy, J.B., Keppie, J.D. and
1269 Hynes, A.J. (eds.), Ancient orogens and modern analogues. Geological Society of
1270 London, Special Publications 327, 215-237.
- 1271
- 1272 Pereira, M.F., Apraiz, A., Chichorro, M., Silva, J.B., Armstrong, R.A., 2010. Exhumation
1273 of high-pressure rocks in northern Gondwana during the Early Carboniferous
1274 (Coimbra-Badajoz-Córdoba shear zone, SW Iberian Massif): Tectonothermal
1275 analysis and U-Th-Pb SHRIMP in-situ zircon geochronology. Gondwana Research
1276 17, 440-460.
- 1277
- 1278 Pereira, M.F., Chichorro, M., Silva, J.B., Ordóñez-Casado, B., Lee, J.K.W., Williams,
1279 I.S., 2012a. Early carboniferous wrenching, exhumation of high-grade metamorphic
1280 rocks and basin instability in SW Iberia: constraints derived from structural geology
1281 and U-Pb and ^{40}Ar - ^{39}Ar geochronology. Tectonophysics 558-559, 28-44.
- 1282
- 1283 Pereira, M.F., Chichorro, M., Moita, P., Santos, J.F., Solá, A.M.R., Williams, I.S., Silva,
1284 J.B., Armstrong, R.A., 2015. The multistage crystallization of zircon in calc-alkaline

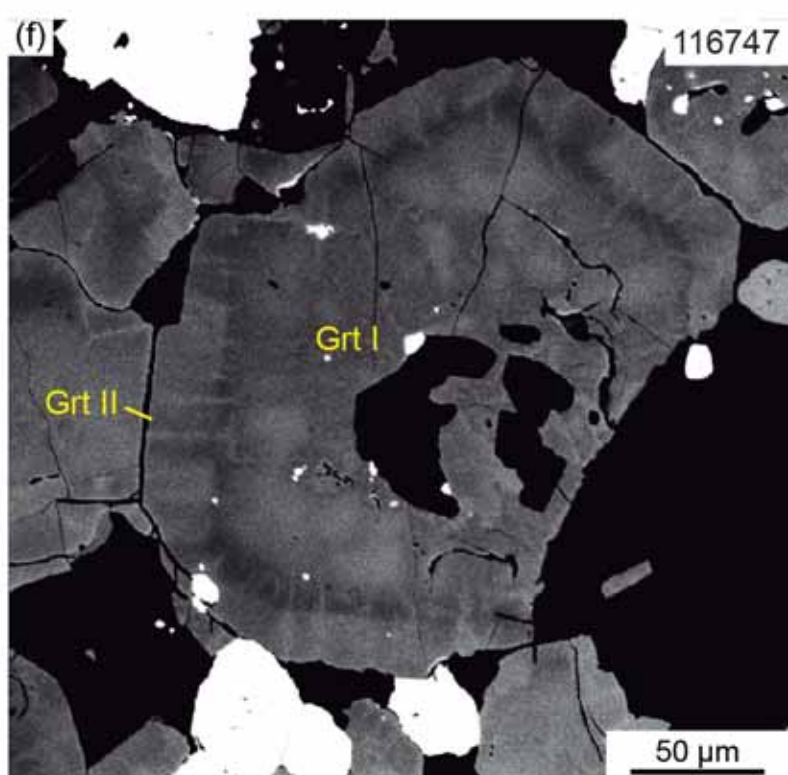
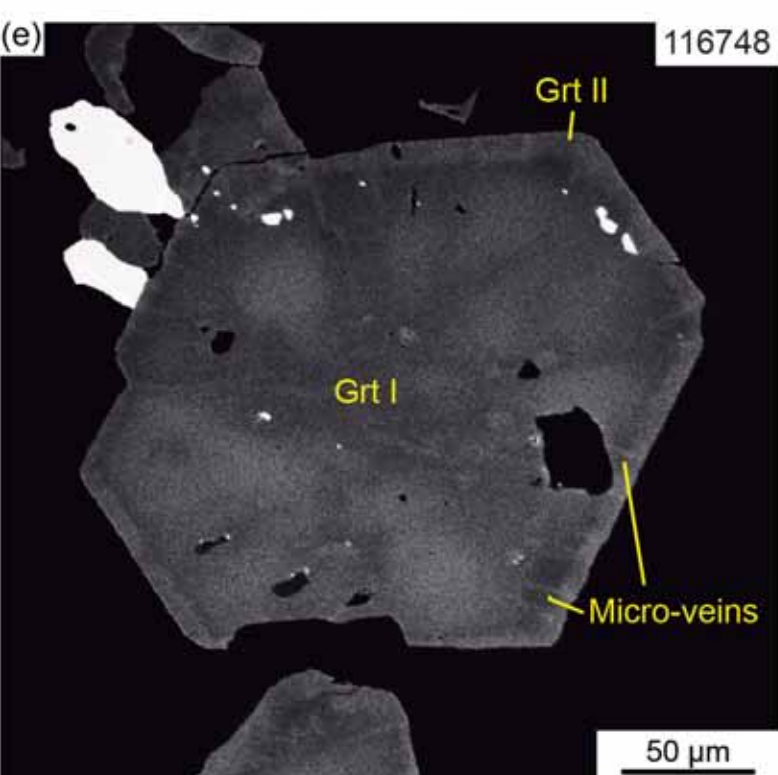
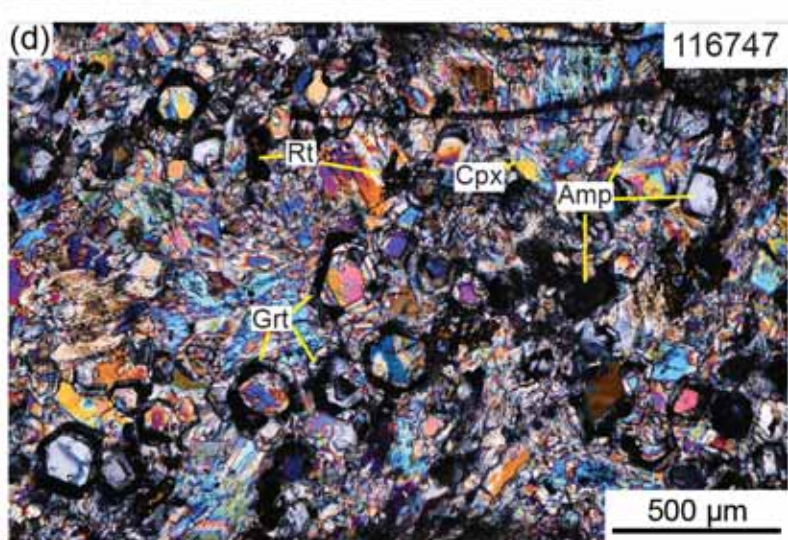
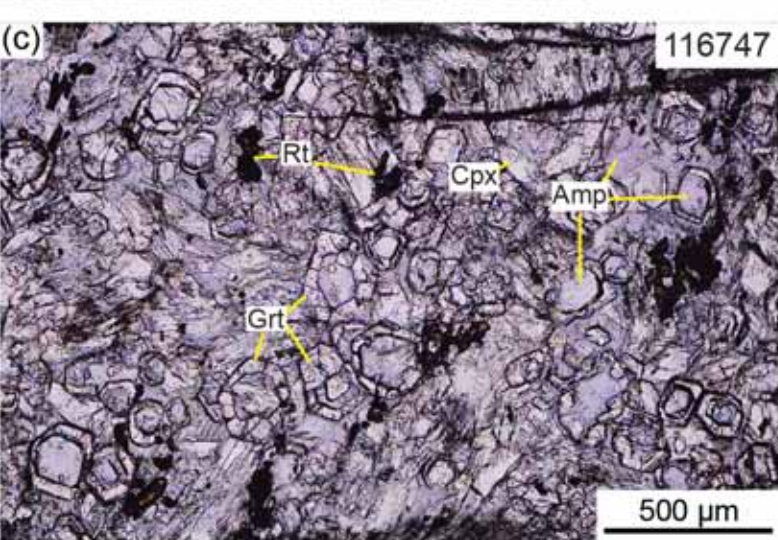
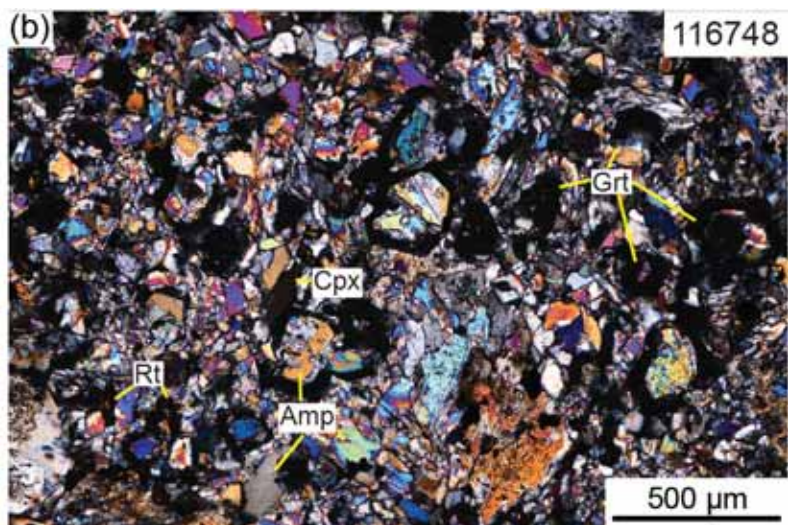
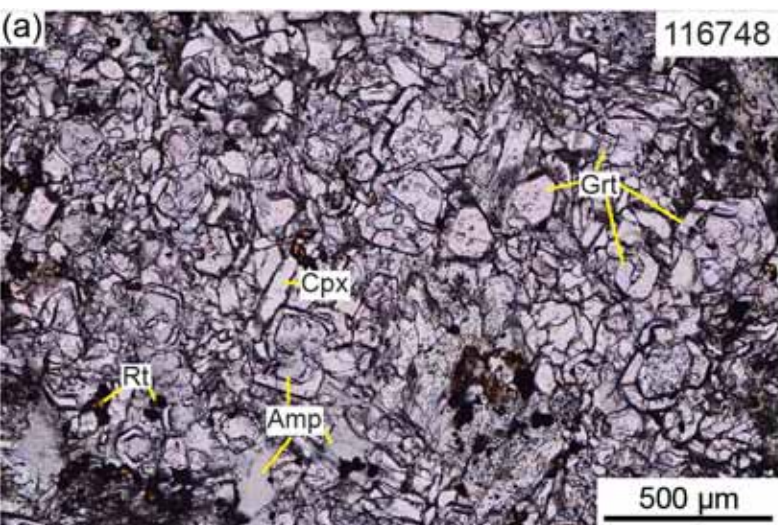
- 1285 granitoids: U-Pb age constraints on the timing of Variscan tectonic activity in SW
1286 Iberia. International Journal of Earth Sciences 104, 1167-1183.
- 1287
- 1288 Puelles, P., Beranoaguirre, A., Ábalos, B, Gil Ibarguchi, J.I., García de Madinabeitia,
1289 S., Rodríguez, J., Fernández-Armas, S., 2017. Eclogite inclusions from subducted
1290 metaigneous continental crust (Malpica-Tui Allochthonous Complex, NW Spain):
1291 Petrofabric, geochronology, and calculated seismic properties. Tectonics 36, 1-31.
- 1292
- 1293 Pouchou, J.L., Pichoir, F., 1985. "PAP" f(4Z) procedure for improved quantitative
1294 microanalysis. In J.T. Armstrong (Ed.), Microbeam analysis (pp. 104-106). San
1295 Francisco Press, San Francisco, CA.
- 1296
- 1297 Ribeiro, A., Munhá, J., Dias, R., Mateus, A., Pereira, E., Ribeiro, L., Fonseca, P.,
1298 Araújo, A., Oliveira, T., Romão, J., Chaminé, H., Coke, C., Pedro, J., 2007.
1299 Geodynamic evolution of the SW Europe Variscides. Tectonics 26, TC6009.
- 1300
- 1301 Rodríguez, J., Cosca, M.A., Gil Ibarguchi, J.I., Dallmeyer, R.D., 2003. Strain
1302 partitioning and preservation of 40Ar/39Ar ages during Variscan exhumation of a
1303 subducted crust (Malpica-Tui Complex, NW Spain). Lithos 70, 111-139.
- 1304
- 1305 Rosas, F.M., 2003. Estudo tectónico do sector de Viana do Alentejo-Alvito: Evolução
1306 Geodinâmica e Modelação Analógica de Estruturas em Afloramentos Chave (Ramo
1307 Sul da Cadeia Varisca Ibérica – SW da Zona de Ossa Morena). Universidade de
1308 Lisboa, PhD thesis, 364 pp.
- 1309
- 1310 Rosas, F.M., Marques, F.O., Ballèvre, M., Tassinari, C., 2008. Geodynamic evolution
1311 of the SW Variscides: Orogenic collapse shown by new tectonometamorphic and
1312 isotopic data from western Ossa-Morena Zone, SW Iberia. Tectonics 27, 1-21.

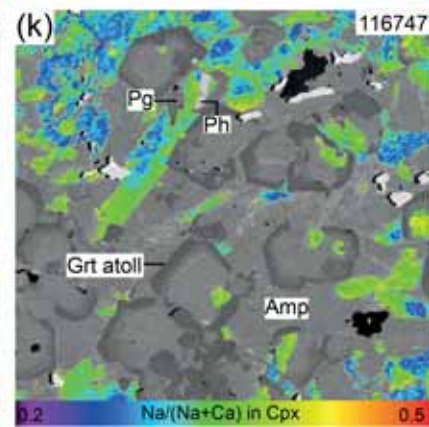
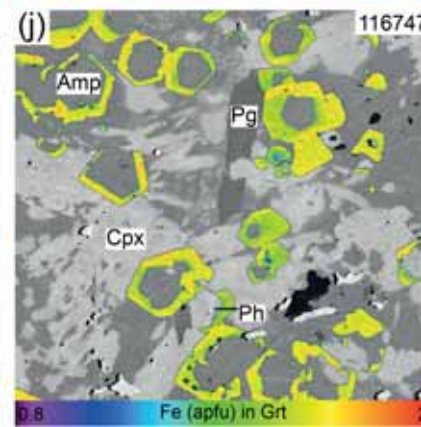
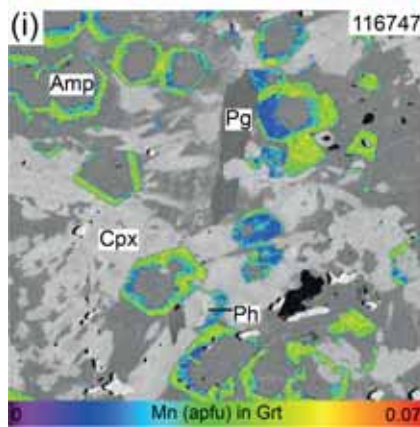
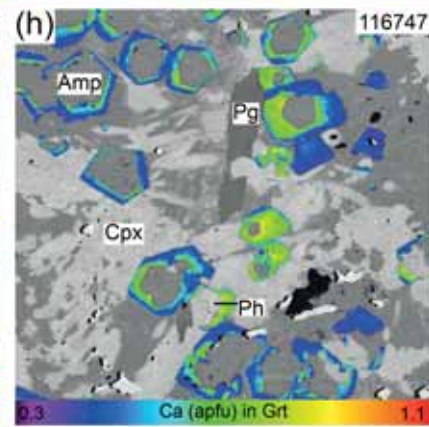
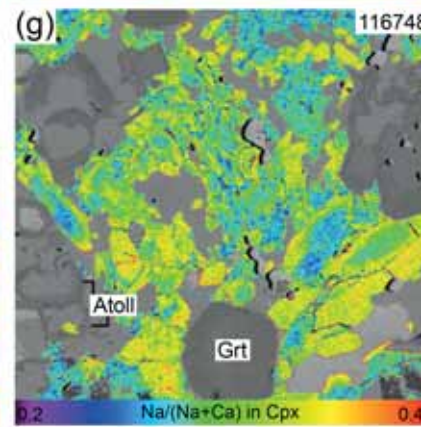
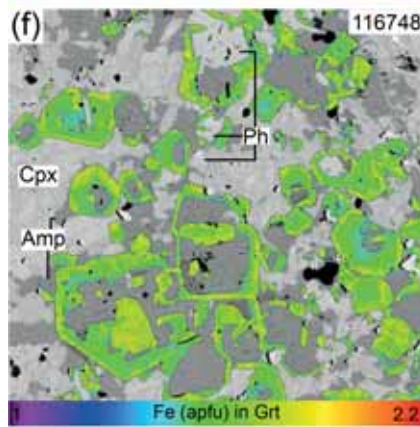
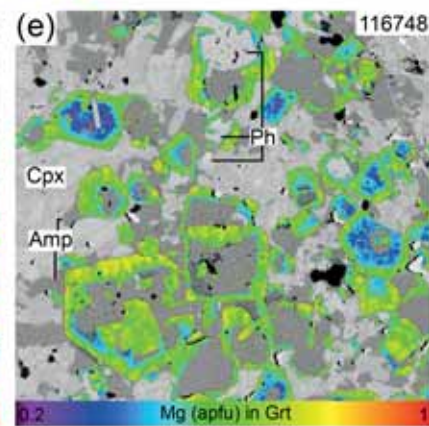
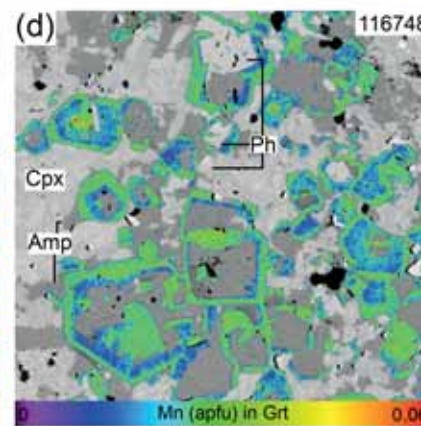
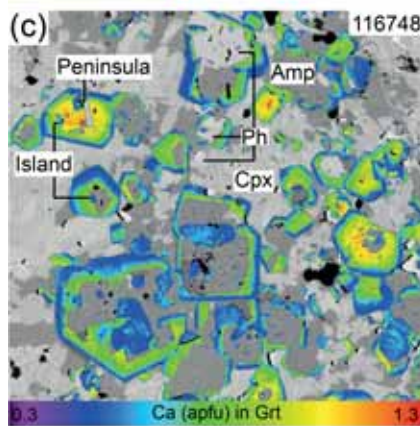
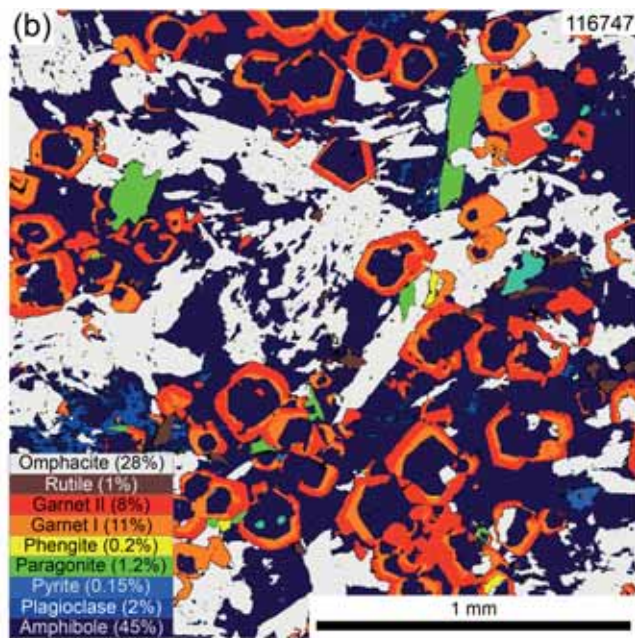
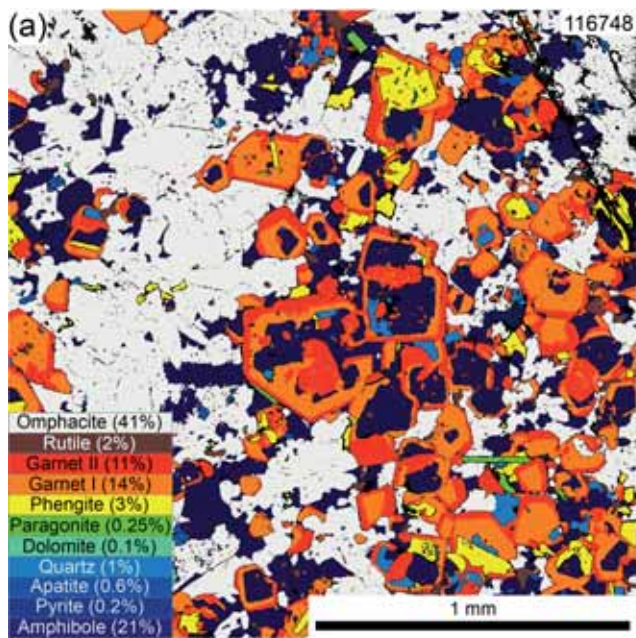
- 1313
- 1314 Rubio Pascual, F.J., Arenas, R., Díaz García, F., Martínez Catalán, J.R., Abati, J.,
1315 2002. Contrasting high-pressure metabasites from the Santiago unit (Órdenes
1316 Complex, northwestern Iberian Massif, Spain), in: Martínez Catalán, J.R., Hatcher,
1317 R.D., Arenas, R., Díaz García, F. (eds), Variscan-Appalachian dynamics: The
1318 building of the late Paleozoic basement. Geological Society of America, Special
1319 Paper 364, 105-124.
- 1320
- 1321 Shervais, J.W., 1982. Ti-V plots and the petrogenesis of modern and ophiolitic lavas.
1322 Earth and Planetary Science Letters 59, 101-108.
- 1323
- 1324 Simancas, J.F., Tahiri, A., Azor, A., Lodeiro, F.G., Poyatos, D.J.M., Hadi, H.E., 2005.
1325 The tectonic frame of the Variscan-Alleghanian orogen in Southern Europe and
1326 Northern Africa. Tectonophysics 398, 181–198.
- 1327
- 1328 Simancas, J.F., Azor, A., Martínez Poyatos, D.J., Expósito Ramos, I., Pérez-Cáceres,
1329 I., González Lodeiro, F. (2016). Comment on “The Late Devonian Variscan suture of
1330 the Iberian Massif: A correlation of high-pressure belts in NW and SW Iberia”.
1331 Tectonophysics 666, 281-284.
- 1332
- 1333 Spiess, R., Peruzzo, L., Prior, D.J., Wheeler, J., 2001. Development of garnet
1334 porphyroblasts by multiple nucleation, coalescence and boundary driven rotations.
1335 Journal of Metamorphic Geology 19, 269-290.
- 1336
- 1337 Sun, S.S., McDonough, W.F., 1989. Chemical and isotopic systematics of oceanic
1338 basalts; implications for mantle composition and processes. Geological Society of
1339 London, Special Publications 42, 313-345.
- 1340

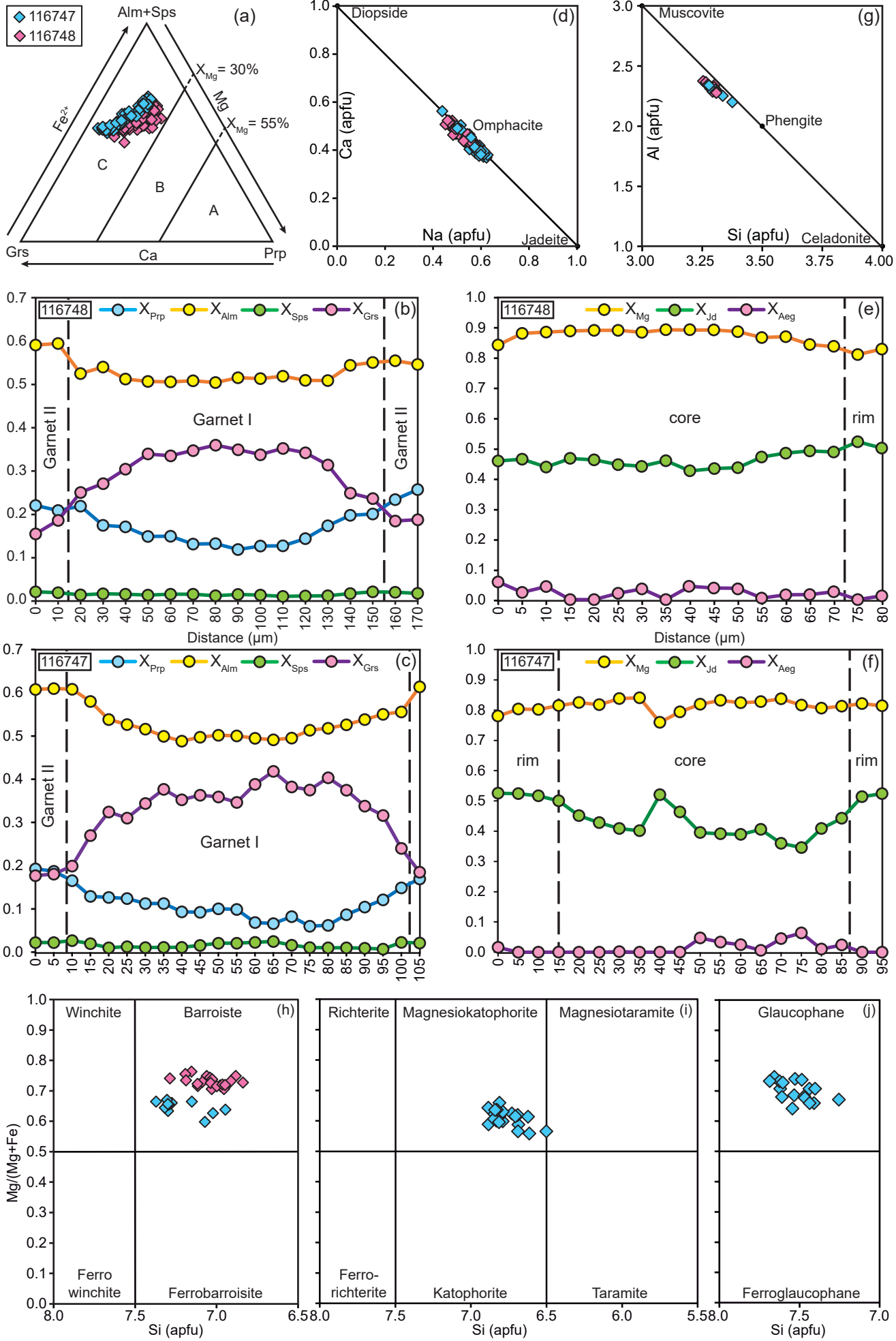
- 1341 Thompson Jr, J.B., 1982. Composition space: an algebraic and geometric approach. In
1342 Ferry J.M. (Ed) Characterization of Metamorphism through Mineral Equilibria,
1343 Mineralogical Society of America: Reviews in Mineralogy 10, 1-31.
- 1344
- 1345 Torres-Roldan, R.L., Garcia-Casco, A., García-Sánchez, P.A., 2000. Cspace: An
1346 integrated workplace for the graphical and algebraic analysis of phase assemblages
1347 on 32-bit Wintel platforms. Computer and Geosciences 26, 779–793
- 1348
- 1349 Torres-Roldán, R.L., García-Casco, A., 2003. DWImager: Una implementación para el
1350 procesamiento de matrices de intercambio de Rayos X. Unpublished document,
1351 Granada University. Available at: <https://www.ugr.es/~agcasco/personal/rx/rx.htm>
- 1352
- 1353 White, R.W., Powell, R., 2002. Melt loss and the preservation of granulites facies
1354 mineral assemblages. Journal of Metamorphic Geology 20, 621-632.
- 1355
- 1356 White, R.W., Powell, R., Holland, T.J.B., 2007. Progress relating to calculation of partial
1357 melting equilibria for metapelites. Journal of Metamorphic Geology 25, 511-527.
- 1358
- 1359 Whitney, D.L., Evans, B.W., 2010. Abbreviations for names of rock-forming minerals.
1360 American Mineralogist 95, 185-187.







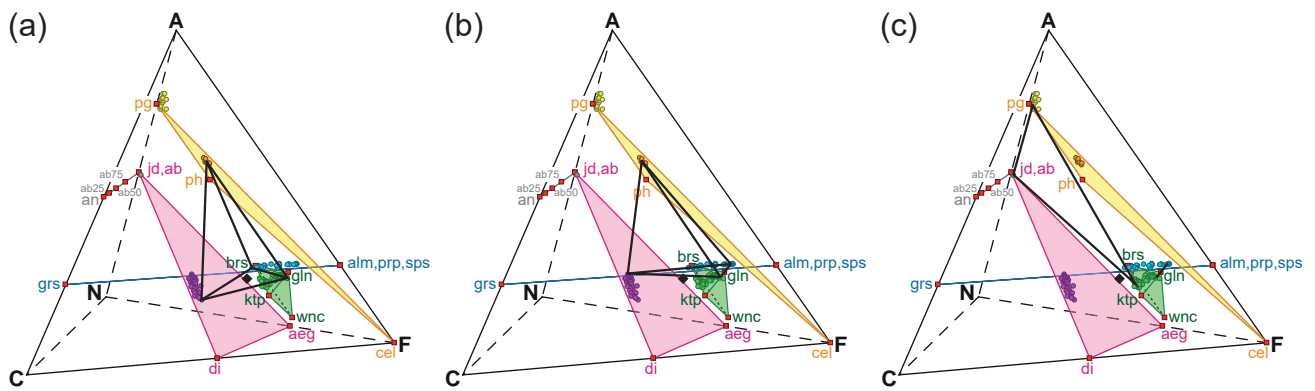




Garnet fracturation & infiltration of fluids

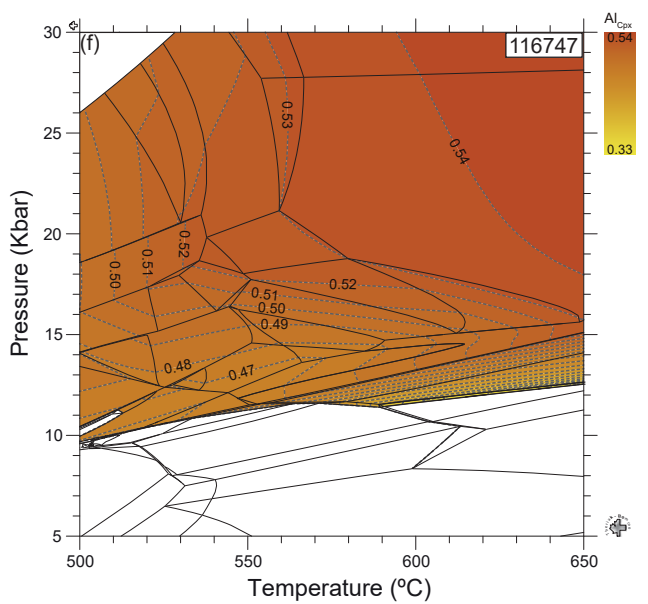
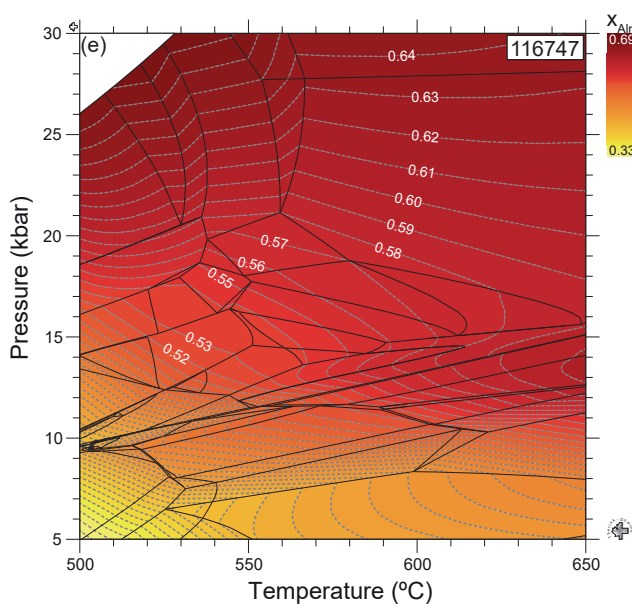
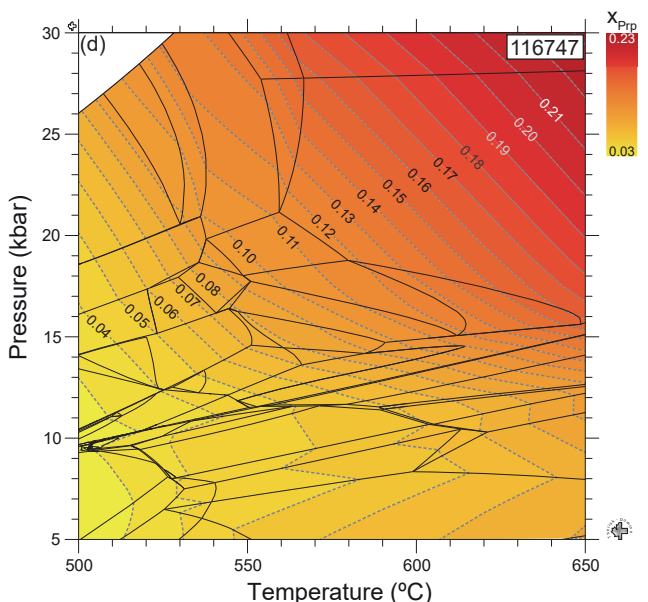
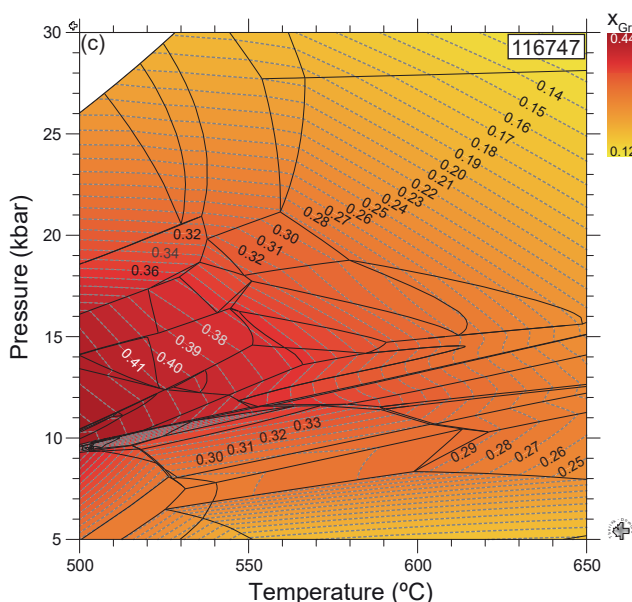
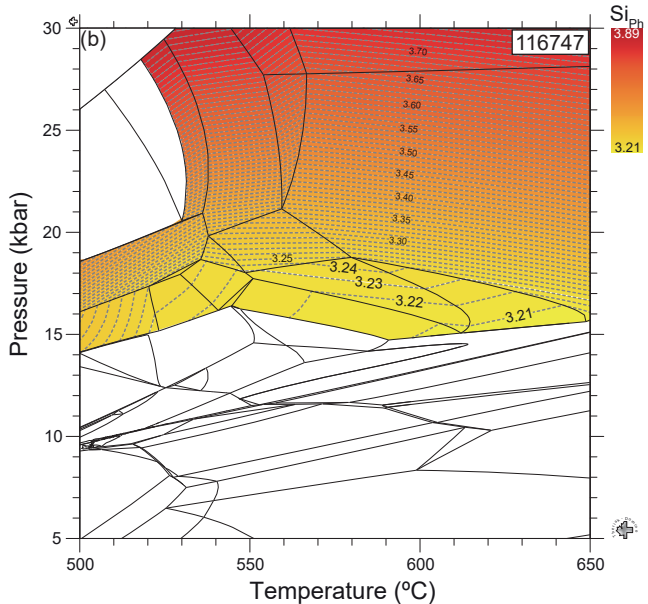
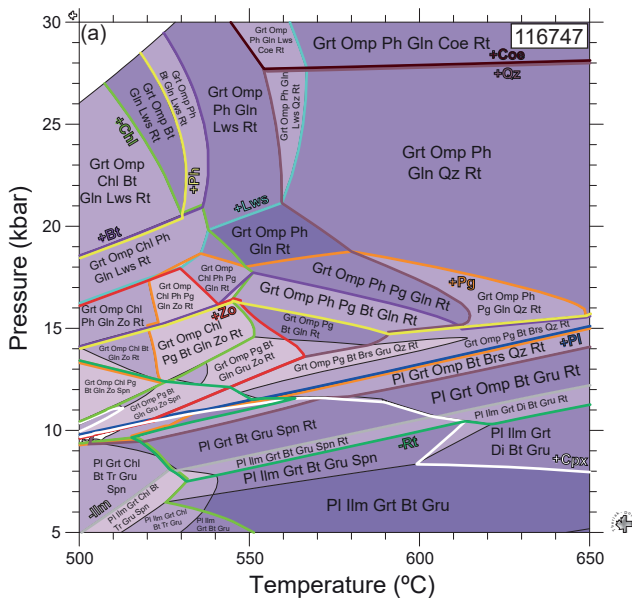
116747

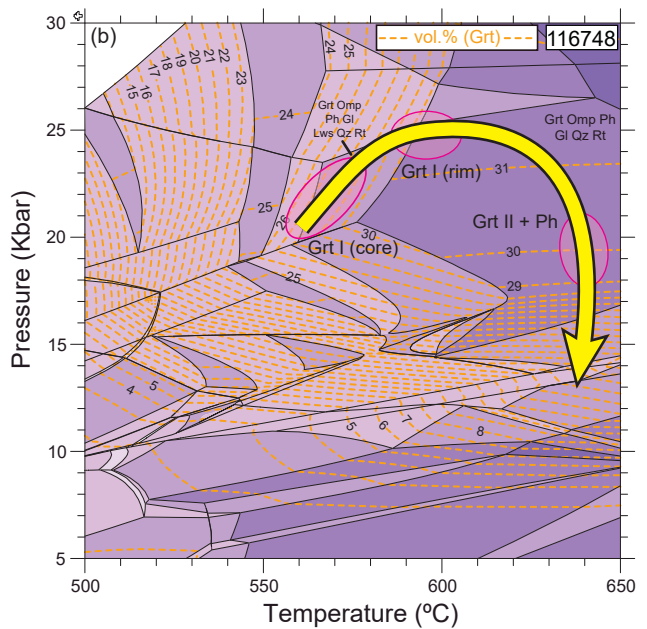
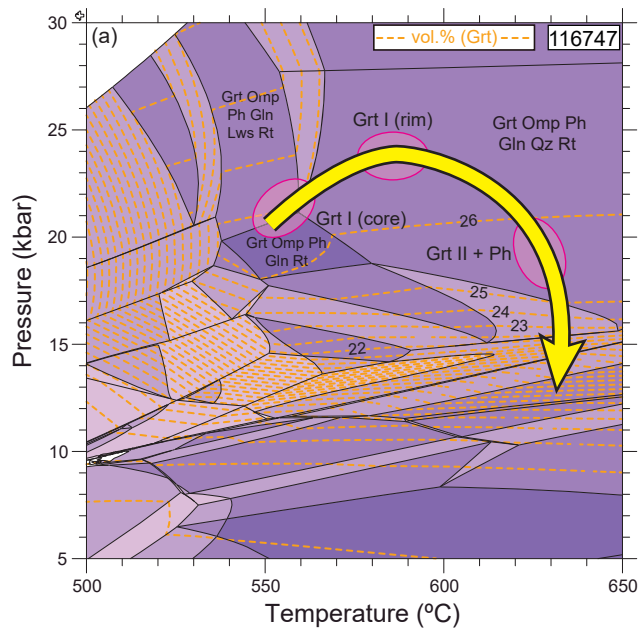
	Stage 1	Stage 2 (peak)	Stage 3	
Garnet	$X_{\text{Grs}}=0.30$ $X_{\text{Ptp}}=0.11$	$X_{\text{Grs}}=0.22$ $X_{\text{Ptp}}=0.15$ $X_{\text{Jd}}=0.37$	$X_{\text{Ptp}}=0.17-0.19$ $X_{\text{Alm}}=0.60-0.61$ $X_{\text{Jd}}=0.55$	$X_{\text{Grs}}=0.19-0.22$
Clinopyroxene		Omp included in Grt I & Core compositions	Inside atoll & Rim composition	
Ca-Na Amphibole				
Phengite	Si = ? Xenoblastic in matrix	Glaucophane in matrix & inside atoll Si = 3.27 - 3.38 apfu	Inside atoll	
Paragonite				
Quartz				
Rutile				
Plagioclase				
Apatite				
Pyrite				

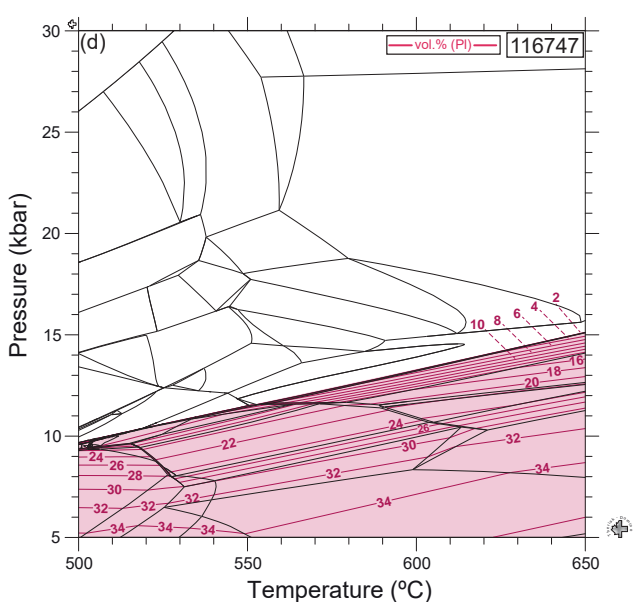
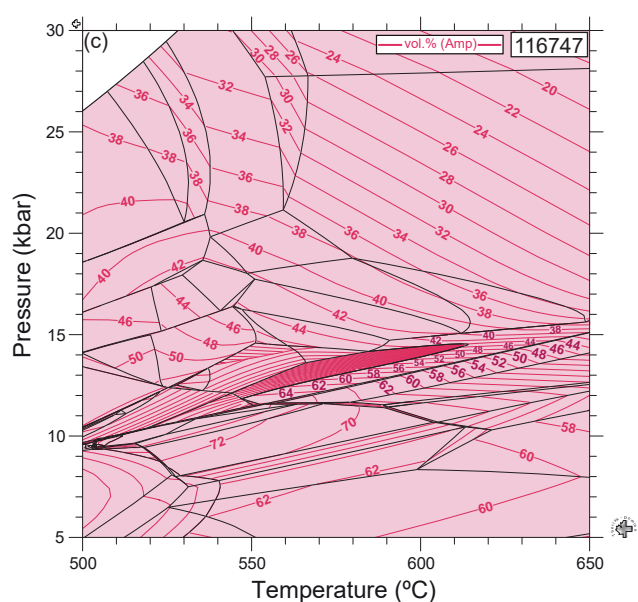
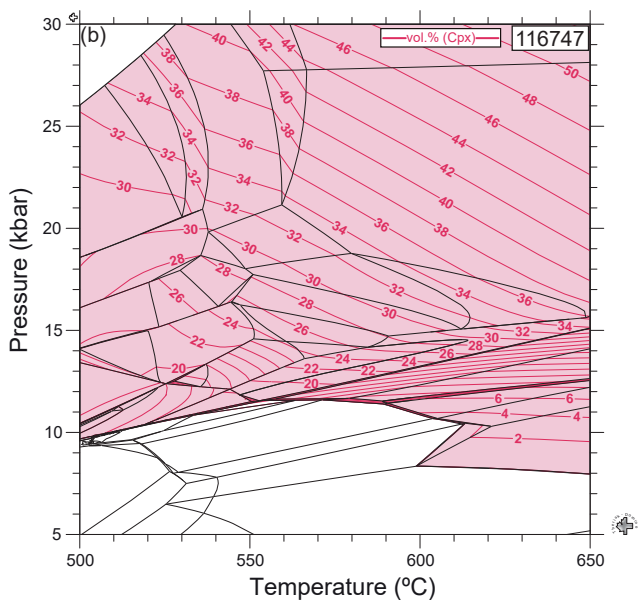
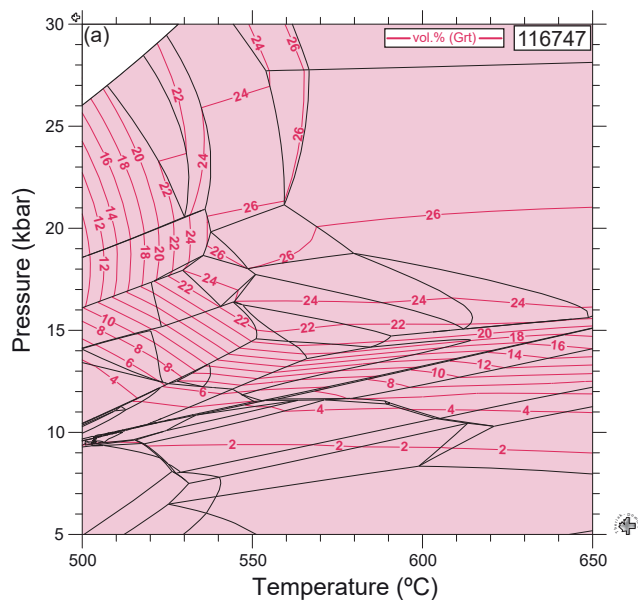


Projection points Exchange vectors: Phases:

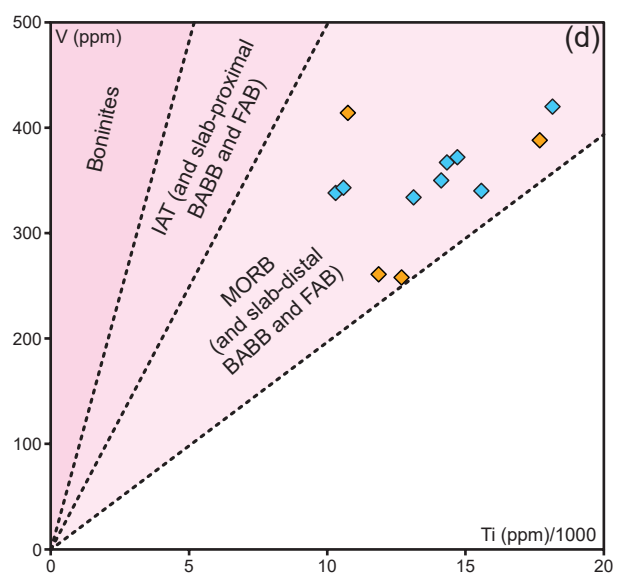
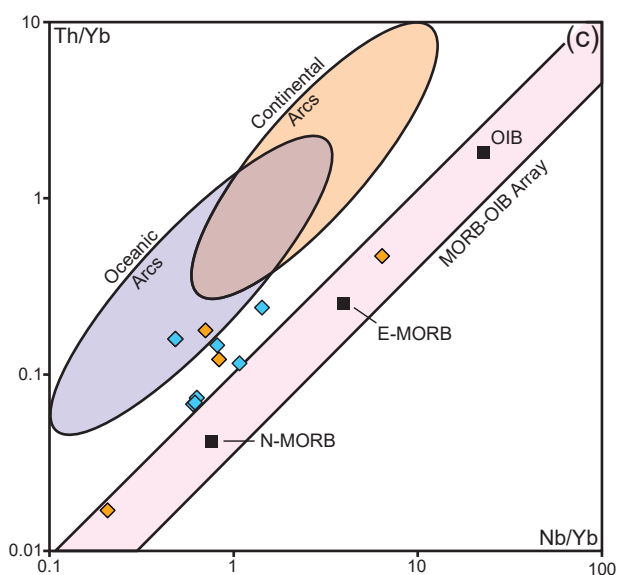
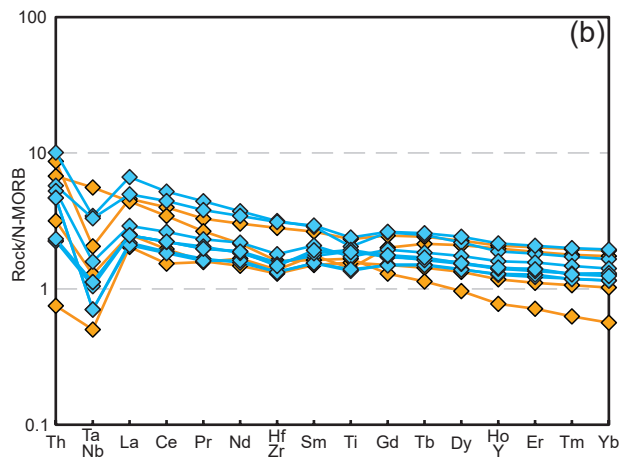
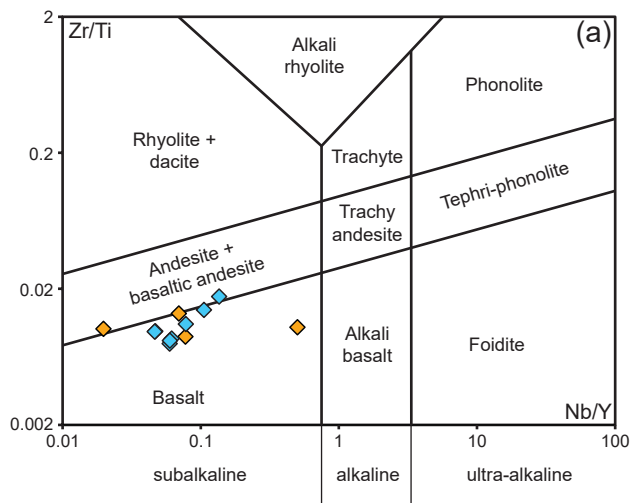
MnFe ₋₁	+Qz
MgFe ₋₁	+Rt
KNa ₋₁	

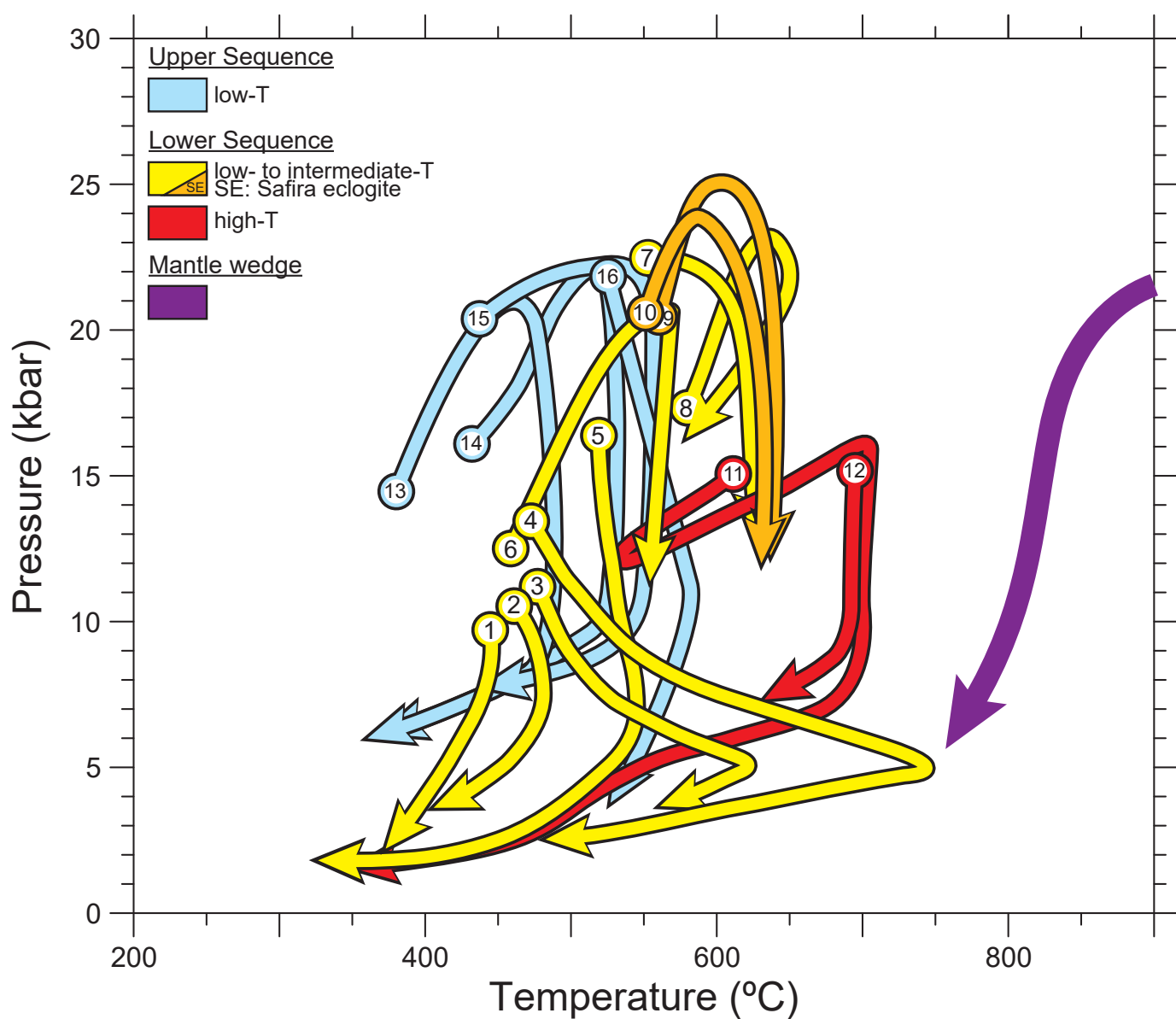






◇ Safira area ◆ Alvito-Viana do Alentejo area





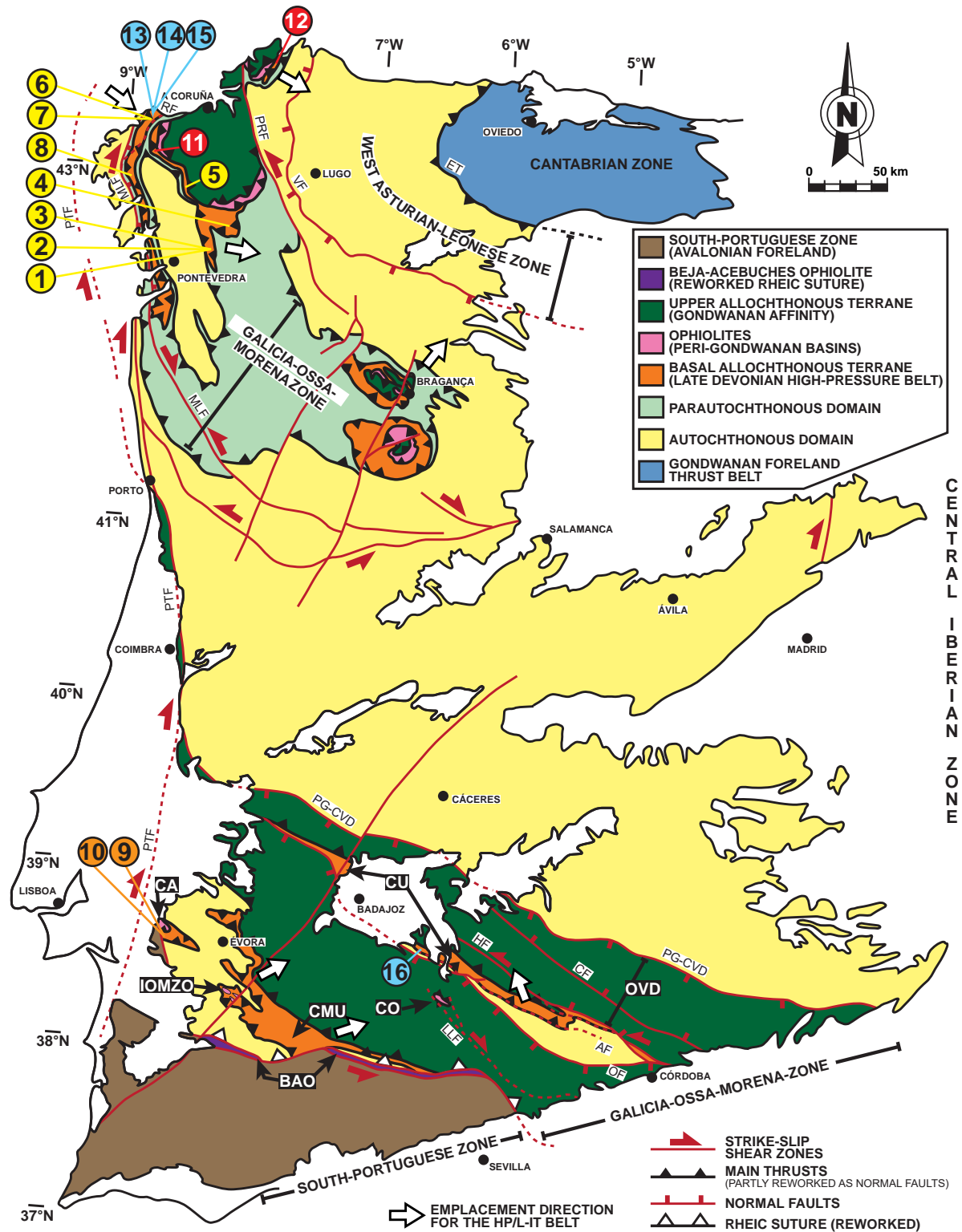


Fig. S1. Thermodynamic modeling of sample 116748

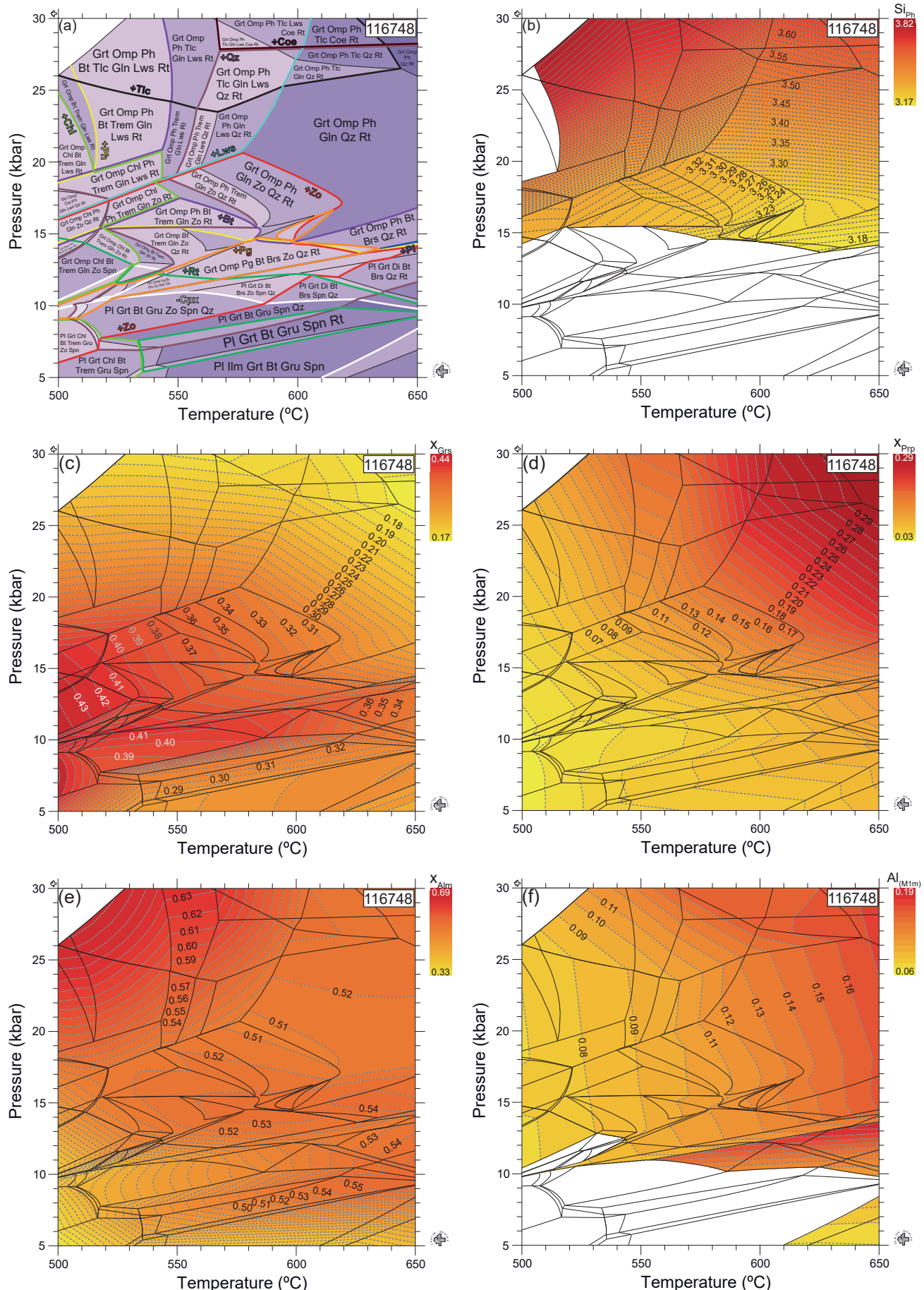


Table 1

Sample	wt.%		MnNCKFMASHT		
	116747	116748	Input	116747	116748
SiO ₂	49.75	48.53	Si	53.55	52.69
TiO ₂	1.98	2.12	Ti	1.6	1.73
Al ₂ O ₃	14.63	15.30	Al	18.56	19.58
FeO	11.50	10.00	Fe	10.35	9.08
MnO	0.22	0.18	Mn	0.2	0.17
MgO	7.03	7.14	Mg	11.28	11.56
CaO	7.31	9.02	Ca	8.43	10.49
Na ₂ O	4.98	3.85	Na	10.39	8.1
K ₂ O	0.16	0.65	K	0.22	0.9
Total	100.20	100.4	H ₂ O	In excess	In excess

Table S1. Representative chemical analysis of garnet.

Sample	116748	116748	116748	116748	116748	116748	116747	116747	116747	116747	116747
Mineral	Grt I	Grt I	Grt I	Grt I	Grt II	Grt II	Grt I	Grt I	Grt II	Grt II	Grt II*
Location	Core	Core	Outermost part	Outermost part	Rim	Rim	Core	Core	Rim	Rim	Rim
Number	42	97	3	15	90	96	184	185	49b	122	189
SiO ₂	38.87	38.54	38.72	39.04	39.18	37.67	37.62	37.43	38.58	38.07	38.03
TiO ₂	0.13	0.15	0.11	0.02	0.00	0.09	0.05	0.03	0.04	0.03	0.03
Al ₂ O ₃	22.19	22.43	22.47	22.80	23.16	23.16	22.91	22.61	22.68	22.69	22.71
FeO _{total}	23.75	23.19	25.44	24.43	23.85	24.21	26.14	26.22	26.92	26.60	26.19
MnO	0.36	0.48	0.42	0.40	0.44	0.40	0.23	0.14	0.73	1.08	0.70
MgO	4.00	3.47	4.36	4.85	6.64	5.52	2.70	2.97	3.82	4.71	4.09
CaO	10.74	12.14	8.83	9.65	7.86	8.59	10.66	10.24	7.65	6.73	7.62
Total	100.05	100.41	100.34	101.20	101.15	99.55	100.44	99.71	100.50	99.97	99.65
Si	3.01	2.98	3.00	2.99	2.98	2.93	2.94	2.95	3.00	2.97	2.98
Ti	0.01	0.01	0.01	0.00	0.00	0.01	0.00	0.00	0.00	0.00	0.00
Al	2.03	2.05	2.05	2.06	2.07	2.12	2.11	2.10	2.08	2.09	2.10
Fe ³⁺	0.00	0.00	0.00	0.00	0.00	0.04	0.00	0.00	0.00	0.00	0.00
Fe ²⁺	1.54	1.50	1.65	1.56	1.51	1.53	1.71	1.72	1.75	1.74	1.72
Mn	0.02	0.03	0.03	0.03	0.03	0.03	0.02	0.02	0.01	0.05	0.05
Mg	0.46	0.40	0.50	0.55	0.75	0.64	0.32	0.35	0.44	0.55	0.48
Ca	0.89	1.01	0.73	0.79	0.64	0.72	0.89	0.86	0.64	0.56	0.64
X _{Ptp}	0.16	0.14	0.17	0.19	0.26	0.22	0.11	0.12	0.15	0.19	0.17
X _{Alm}	0.53	0.51	0.57	0.53	0.52	0.53	0.58	0.59	0.61	0.59	0.61
X _{Sps}	0.01	0.01	0.01	0.01	0.01	0.01	0.01	0.00	0.02	0.02	0.03
X _{Grs}	0.31	0.34	0.25	0.27	0.22	0.23	0.30	0.29	0.22	0.19	0.22

Table S2. Representative chemical analysis of clinopyroxene.

Sample	116748	116748	116748	116748	116748	116748	116748	116748	116747	116747	116747	116747	116747	116747
Mineral	Cpx													
Location	Core	Core	Core	Rim	Rim	Rim	Core	Core	Core	Core	Rim	Rim	Rim	Rim
Number	150p*	152p*	111	53	145p*	148p*	142	182p*	205	173p*	151	192p*	151	192p*
SiO ₂	56.12	56.34	55.08	56.50	56.11	56.25	55.87	56.03	55.28	56.42	55.06	56.53	56.53	56.53
TiO ₂	0.07	0.01	0.09	0.08	0.05	0.10	0.03	0.03	0.06	0.07	0.19	0.06	0.06	0.06
Al ₂ O ₃	10.30	10.05	11.13	12.75	11.79	13.31	11.68	11.04	11.16	12.89	13.35	12.66	12.66	12.66
FeO	4.04	4.22	4.25	2.75	3.47	3.59	3.86	3.72	4.43	3.60	3.88	2.96	2.96	2.96
MgO	8.99	8.97	8.78	8.29	7.85	6.47	8.37	8.05	7.84	7.17	7.23	7.40	7.40	7.40
CaO	14.93	14.24	13.06	12.26	13.04	10.63	12.63	13.45	12.68	11.83	11.09	11.32	11.32	11.32
Na ₂ O	6.36	6.20	6.94	7.50	7.09	8.07	7.50	6.58	7.17	7.86	8.38	7.27	7.27	7.27
Total	100.83	100.14	99.33	100.12	99.45	98.61	99.93	98.95	98.62	99.93	99.31	98.38	98.38	98.38
Si	1.99	2.00	1.97	1.99	2.00	2.01	1.98	2.01	1.99	1.99	1.96	2.01	2.01	2.01
Ti	0.00	0.00	0.00	0.00	0.00	0.00	0.00	0.00	0.00	0.00	0.01	0.00	0.00	0.00
Al	0.43	0.42	0.47	0.53	0.49	0.56	0.49	0.47	0.47	0.54	0.56	0.53	0.53	0.53
Fe ³⁺	0.04	0.00	0.09	0.01	0.00	0.00	0.09	0.00	0.05	0.05	0.02	0.00	0.00	0.00
Fe ²⁺	0.08	0.13	0.04	0.07	0.10	0.11	0.03	0.11	0.08	0.09	0.12	0.09	0.09	0.09
Mg	0.47	0.48	0.47	0.43	0.42	0.34	0.44	0.43	0.42	0.38	0.38	0.39	0.39	0.39
Ca	0.57	0.54	0.50	0.46	0.50	0.41	0.48	0.52	0.49	0.45	0.42	0.43	0.43	0.43
Na	0.44	0.43	0.48	0.51	0.49	0.56	0.52	0.46	0.50	0.54	0.58	0.50	0.50	0.50
Jd	39.77	42.78	41.15	50.43	49.03	45.18	44.16	46.36	45.29	52.52	48.93	52.38	52.38	52.38

Table S3. Representative chemical analysis of amphibole.

Sample	116748	116748	116748	Brs	Brs	Brs	Brs	Brs	Gln	Gln	Gln	Gln	Brs	Mkt	Brs
Mineral															
Number	39	49	103		109	113		114		163	176	201	121	145	207
SiO ₂	48.90	49.23	51.12		50.89	48.63		49.19		52.67	54.47	52.36	52.12	45.26	49.13
TiO ₂	0.34	0.30	0.22		0.20	0.45		0.38		0.16	0.14	0.15	0.16	0.27	0.69
Al ₂ O ₃	14.51	13.89	13.57		13.55	14.30		14.38		13.88	13.30	13.43	13.74	15.69	13.89
FeO	9.56	9.51	9.10		8.98	9.41		9.70		8.70	9.19	10.61	9.93	12.56	11.78
MgO	11.63	12.35	12.05		11.95	12.08		11.93		10.20	10.23	9.81	10.24	9.85	10.23
CaO	6.80	5.82	4.05		4.54	6.69		6.16		2.21	1.46	2.20	3.19	7.06	5.73
Na ₂ O	4.69	5.12	6.06		6.06	4.72		5.34		7.20	7.40	6.77	6.44	4.83	5.37
K ₂ O	0.28	0.26	0.19		0.26	0.29		0.26		0.14	0.08	0.10	0.11	0.29	0.17
Total	96.87	96.66	96.55		96.51	96.86		97.52		95.38	96.34	95.63	96.18	96.13	97.20
Si	6.95	6.98	7.19		7.19	6.91		6.95		7.47	7.61	7.44	7.37	6.62	7.02
Ti	0.04	0.03	0.02		0.02	0.05		0.04		0.02	0.01	0.02	0.02	0.03	0.07
Al	2.43	2.32	2.25		2.25	2.40		2.39		2.32	2.19	2.25	2.25	2.71	2.34
Fe ³⁺	0.11	0.26	0.25		0.15	0.18		0.16		0.00	0.07	0.19	0.09	0.19	0.11
Fe ²⁺	1.01	0.80	0.76		0.87	0.90		0.94		1.03	0.99	1.04	1.07	1.30	1.27
Mg	2.46	2.61	2.53		2.52	2.56		2.51		2.15	2.13	2.08	2.16	2.15	2.18
Ca	1.04	0.88	0.61		0.69	1.02		0.93		0.34	0.22	0.34	0.48	1.11	0.88
Na	1.29	1.41	1.65		1.66	1.30		1.46		1.98	2.00	1.87	1.77	1.37	1.49
K	0.05	0.05	0.03		0.05	0.05		0.05		0.02	0.01	0.02	0.02	0.05	0.03
^v Al(C)	1.39	1.30	1.44		1.44	1.31		1.34		1.79	1.80	1.68	1.66	1.33	1.36
Na(B)	0.94	1.05	1.33		1.27	0.94		1.03		1.66	1.76	1.62	1.50	0.83	1.09
Mg#	0.71	0.75	0.75		0.73	0.73		0.72		0.68	0.68	0.66	0.67	0.61	0.63

Table S4. Representative chemical analysis of white mica and plagioclase.

Sample	116748	116748	116748	116748	116748	116747	116747	116747	116747	116747	116747	116747
Mineral	Ph	Ph	Ph	Pg	Pg	Ph	Ph	Pg	Pg	Ph	Pg	Ph
Number	59	68	86	60	64	131	168	193	134	181	119	213
SiO ₂	49.46	49.87	48.51	45.71	47.14	49.99	49.26	48.44	46.07	45.46	67.35	66.72
TiO ₂	0.40	0.66	0.57	0.17	0.16	0.47	0.48	0.59	0.15	0.08	0.00	0.00
Al ₂ O ₃	29.11	29.17	30.03	41.33	40.46	27.63	28.21	29.43	40.60	40.73	20.36	20.14
FeO	1.69	1.73	1.53	0.57	0.51	2.01	1.85	1.84	0.44	0.42	0.27	0.23
MgO	3.30	3.35	3.15	0.22	0.21	3.47	3.57	3.14	0.12	0.13	0.05	0.00
CaO	0.00	0.00	0.00	0.26	0.16	0.00	0.00	0.06	0.12	0.14	0.36	0.26
Na ₂ O	0.94	1.02	0.98	6.89	6.78	0.74	0.74	1.07	7.60	7.46	11.97	12.01
K ₂ O	9.31	9.01	9.24	0.83	1.07	8.86	8.65	8.62	0.64	0.52	0.02	0.00
Total	94.56	95.06	94.42	96.13	96.55	93.39	93.03	93.54	95.93	95.10	100.48	99.50
Si	3.31	3.31	3.25	2.90	2.98	3.38	3.34	3.27	2.93	2.92	2.94	2.94
Ti	0.02	0.03	0.03	0.01	0.01	0.02	0.02	0.03	0.01	0.00	0.00	0.00
Al	2.30	2.28	2.37	3.10	3.01	2.20	2.25	2.34	3.05	3.08	1.05	1.05
Fe	0.09	0.10	0.09	0.03	0.03	0.11	0.11	0.10	0.02	0.02	0.01	0.01
Mg	0.33	0.33	0.31	0.02	0.02	0.35	0.36	0.32	0.01	0.01	0.00	0.00
Ca	0.00	0.00	0.00	0.02	0.01	0.00	0.00	0.00	0.01	0.01	0.02	0.01
Na	0.12	0.13	0.13	0.85	0.83	0.10	0.10	0.14	0.94	0.93	1.01	1.03
K	0.79	0.76	0.79	0.07	0.09	0.76	0.75	0.74	0.05	0.04	0.00	0.00
									An	1.65	1.16	
									Ab	98.23	98.84	
									Kfs	0.12	0.00	

Table S5. Whole rock analysis of major (wt%) and trace elements (ppm) from the high-P rocks samples of the Safira and Alvito-Viana do Alentejo areas (CMU).

Sample Location	116742	116743	116747	116748	116751	116752	116753	116754	116755	116756	116757	116758
	Safira area				Alvito-Viana do Alentejo area							
SiO ₂	50.38	51.28	49.75	48.53	49.20	52.78	49.66	52.67	50.57	51.58	49.26	49.45
TiO ₂	1.76	2.95	1.98	2.12	2.39	2.60	3.03	2.19	1.72	1.77	2.45	2.36
Al ₂ O ₃	13.61	13.59	14.63	15.30	14.31	13.50	12.67	13.07	13.85	13.87	14.13	14.31
Fe ₂ O ₃	1.85	1.37	1.05	2.13	4.20	1.53	1.73	1.47	3.96	4.89	4.99	4.78
FeO	9.30	13.60	11.50	10.00	9.40	11.40	13.10	11.80	8.20	6.90	8.40	8.80
MnO	0.12	0.25	0.22	0.18	0.29	0.28	0.28	0.25	0.19	0.16	0.24	0.22
MgO	8.74	4.75	7.03	7.14	5.78	4.17	5.27	4.68	6.24	6.26	5.51	5.81
CaO	6.67	7.09	7.31	9.02	7.05	7.00	7.56	8.24	8.40	8.38	7.64	7.36
Na ₂ O	3.41	4.38	4.98	3.85	4.40	4.89	3.94	3.94	2.59	2.69	4.11	4.40
K ₂ O	0.90	0.08	0.16	0.65	0.35	0.15	0.04	0.08	0.15	0.22	0.05	0.09
P ₂ O ₅	0.23	0.30	0.20	0.23	0.27	0.37	0.40	0.25	0.14	0.14	0.28	0.31
LOI	2.19	-0.77	0.14	0.11	1.63	-0.33	0.13	-0.33	2.27	1.97	1.30	1.10
Total	100.20	100.40	100.20	100.40	100.30	99.61	99.27	99.63	99.20	99.60	99.30	99.97
Na ₂ O+K ₂ O	4.31	4.46	5.14	4.50	4.75	5.04	3.98	4.02	2.74	2.91	4.16	4.49
Mg#	0.48	0.26	0.38	0.42	0.38	0.27	0.29	0.28	0.43	0.48	0.40	0.40
V	414	388	261	258	367	340	420	334	338	343	372	350
Y	55.7	59	33.5	21.5	39	53	60.5	44.9	36.2	36.6	40.3	40.1
Zr	107	232	105	132	123	272	253	144	100	102	116	117
Nb	1.1	4.1	2.6	11	2.4	7.2	6.4	3.5	1.7	1.7	2.4	2.4
La	5.09	11.5	6.27	11	6.19	16.6	12.4	7.25	5.46	5.24	6.19	6.19
Ce	11.5	29.9	14.7	25.8	16.7	39	33.2	19.7	14.1	13.7	16.6	16.7
Pr	2.08	4.33	2.11	3.51	2.61	5.83	5.02	3.06	2.2	2.12	2.7	2.61
Nd	12.2	22.1	10.8	15.7	13.8	27.2	25.1	16	11.4	11.8	13.4	13.7
Sm	4.62	6.93	3.94	4.29	4.59	7.54	7.69	5.47	4.06	4.07	4.81	5.05
Gd	7.38	9.07	5.52	4.76	6.31	9.58	9.67	7.14	5.55	5.47	6.43	6.51
Tb	1.44	1.62	0.96	0.76	1.11	1.67	1.72	1.24	1.01	1	1.09	1.14
Dy	9.55	10.3	6.07	4.38	7.11	9.98	11	7.95	6.35	6.3	6.96	7.02
Ho	2	2.08	1.17	0.79	1.43	1.89	2.18	1.6	1.26	1.29	1.39	1.45
Er	5.57	6	3.29	2.12	4.18	5.4	6.16	4.65	3.63	3.78	4.01	4.14
Tm	0.812	0.894	0.486	0.286	0.587	0.787	0.909	0.672	0.541	0.538	0.59	0.582
Yb	5.31	5.83	3.12	1.72	3.89	5.05	5.95	4.3	3.52	3.52	3.98	3.8
Hf	2.7	5.1	2.4	2.9	3	5.4	5.7	3.4	2.7	2.6	3	2.8
Ta	0.07	0.31	0.19	0.85	0.14	0.5	0.51	0.22	0.09	0.09	0.16	0.16
Th	0.09	1.04	0.38	0.81	0.27	1.21	0.69	0.63	0.56	0.56	0.27	0.28
Nb/Y	0.020	0.069	0.078	0.512	0.062	0.136	0.106	0.078	0.047	0.046	0.060	0.060
Zr/Ti	0.010	0.013	0.009	0.010	0.009	0.017	0.014	0.011	0.010	0.010	0.008	0.008
Nb/Yb	0.207	0.703	0.833	6.395	0.617	1.426	1.076	0.814	0.483	0.483	0.603	0.632
Th/Yb	0.017	0.178	0.122	0.471	0.069	0.240	0.116	0.147	0.159	0.159	0.068	0.074
Ti/1000	10.749	17.685	11.858	12.685	14.328	15.575	18.147	13.117	10.305	10.581	14.706	14.124
V/Ti	0.039	0.022	0.022	0.020	0.026	0.022	0.023	0.025	0.033	0.032	0.025	0.025